Light Absorption Enhancement with Bio-inspired Nanostructures

Final report

Authors: J.M. Llorens[1], T. Vasileiou[2], A. Raya[1], J. Buencuerpo[1], J. M. Ripalda[1], K. Hildebrant[2], D. Izzo[2], L. Summerer[2]

Affiliation:
[1]IMN Institute of Micro and Nanotechnology (IMN-CNM-CSIC),
[2]Advanced Concepts Team, European Space Agency (ESA)

Date: 15/12/2020

Contacts:

Jose M. Llorens (Research fellow IMN)
Tel: +34 91 8372211
Fax: +34 91 8060701
e-mail: jose.llorens@csic.es

Leopold Summerer (Technical Officer)
Tel: +31(0)715654192
Fax: +31(0)715658018
e-mail: act@esa.int

Available on the ACT website
http://www.esa.int/act

Ariadna ID: 19/1902
Ariadna study type: Standard
Contract Number: 4000127654/19/NL/AS

Light Absorption Enhancement with Bio-inspired Nanostructures for Space Solar Cells

Abstract

In this study we aims to describe bio-inspired and industrially scalable advanced concepts for increasing the end of life efficiency of space solar cells. More specifically, this report is concerned with the structure of the dielectric layers in between the semiconductor and the cover glass. By scattering light with dielectric nanostructures, reflection losses can be reduced and at the same time the effective optical path length inside the semiconductor can be made larger than the semiconductor layer thickness. This should allow for reduced device thickness and consequently lead to a lower sensitivity to the reduced diffusion lengths resulting from radiation damage.

The starting point for this exploratory study has been inspired by biological structures optimized by natural selection such as diatoms and moth eyes.

The most striking result is the possibility to reduce the thickness of the InGaAs layer of a prototypical space solar cell from 1.8 µm to 0.5 µm without sacrificing efficiency. Special emphasis is put in describing the impact of the middle junction thinning on the end of life efficiency.

We have also found that in addition to a light-trapping structure beneath the cover glass, a spectrally selective mirror of very high reflectance is important. Realistic proposals critically review the penalty introduced when non-ideal systems are introduced.

We consider the results of this research promising to integrate the technology roadmap of the European space photovoltaic industry.

1 Introduction

Innovation in solar cells for space is a very active field. One of the main lines of work is at the device level. The three main technologies to achieve higher efficiencies are lattice-matched epitaxy, upright metamorphic and inverted metamorphic combining either three or four junctions. Figure 1 shows the roadmap of Azur Space Solar Power GmbH, the main European producer of solar cells for space. The roadmap identifies the maturity of each technology together with its performance and suitability for different orbits altitudes. Currently, the solar cell efficiency at the beginning of life (BOL) lays between 30% and 32%.

A major problem that solar cells are facing in space is the reduction in the end of life (EOL) efficiency. One of the main causes is the creation of defects by high energy particles. The minority carriers diffusion length is reduced due to the scattering with the newly created defects impacting the collection efficiency. A direct way to enhance the EOL is by thinning the thickness of the junctions. However, this approach has a great penalty in the light being absorbed and thus in the efficiency. Our proposal is to introduce a photonic structure between the top surface and the cover glass to bend the light away from the solar cell normal and hence increase the optical-path length. In addition, it is also possible to couple the incoming light with the natural guided modes of the layer stack, resulting in its total absorption. The combination of these type of techniques with solar cells to increase the absorption is known as *light-trapping techniques*. An additional benefit is

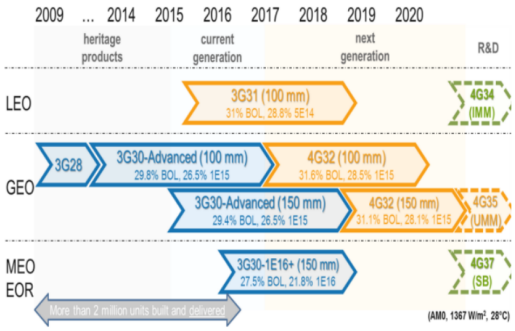

Figure 1: Azur's roadmap of the development of future solar cells for LEO, GEO and MEO missions. Colors indicate the technology employed in the device fabrication: (blue) lattice-matched, (orange) upright metamorphic and (green) inverted metamorphic. Extracted from Ref. [1]

the possibility to reduce the reflection losses, meaning that no additional anti-reflective coating treatment would be needed in the solar cell.

In this study, we focus on the prototypical space solar cell, the 3G30. It is a very mature technology as can be seen in Figure 1. The solar cell consists of three junctions fitted for the bandgaps 1.9, 1.4 and 0.66 eV. The three junctions comprise GaInP, InGaAs and Ge semiconductors, respectively. The most critical junction is the InGaAs layer [2]. Substantial efforts are made to try to reduce its thickness. [3, 4, 5]. A cross-section of the solar cells is reproduced in Figure 2(a).

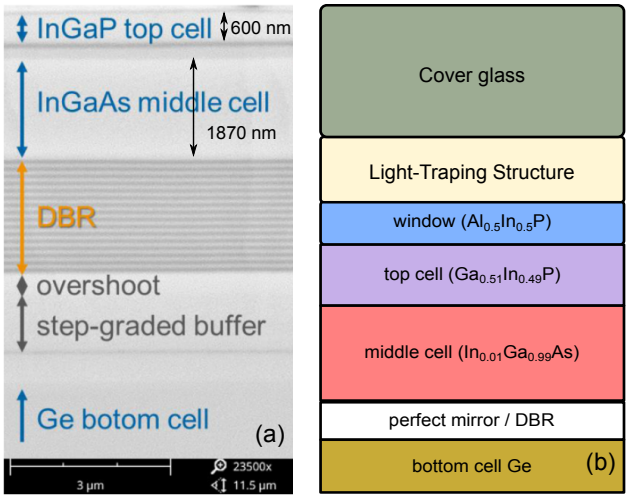

Figure 2: (a) TEM cross-section of 3G30 solar cell. Extracted from [1]. The thickness of the top and middle junction have been determined graphically using the scale at the bottom. (b) Model of the 3G30 used in the optimization and cell characterization.

The thickness of the top and middle junction has been determined graphically using the scale displayed at the bottom. The material concentration is not provided in [1]. It has been set by searching for the lattice match ternary to the Ge substrate. The overshoot step-graded buffer may introduce some deviations to the actual values. A distributed Bragg reflector (DBR) is placed between the bottom junction and the other two junctions. It is a dielectric mirror introduced to reflect the light of energy greater than that of the middle cell (1.4 eV). The luminescence from the

middle junction is reflected back into the top junctions.

The model for this device is shown in Fig. 2(b). We consider a cover glass which plays the role of a front media, i.e. a semi-infinite space in which the solar light is propagating. Next, we place the light-trapping structure which is described in the next Section. For simplicity, we have ignored here the encapsulant material usually found between the solar cell and the cover glass. The refractive index contrast between the encapsulant layer and the cover glass is very small and therefore it is justified to disregard it from the optical analysis, the main objective of the current study. The rest of the layers are part of the solar cell. The first layer in the solar cell is the *window* layer to prevent the recombination of carriers at the top interface. Its thickness is kept fixed to 15 nm being its composition $Al_{0.5}In_{0.5}P$. The top and middle cell are two homogeneous layers: $Ga_{0.49}In_{0.50}P$ and $In_{0.01}Ga_{0.99}As$, respectively. If not stated otherwise, we will considered as reference thicknesses the values reported in Fig. 2(a). Finally, at the bottom is the Ge substrate.

In between the middle and bottom junction we consider the effect of an interstitial mirror. As a first approximation, the effect of the DBR is modelled as a spectrally selective perfect mirror (SPM) an ideal material with large dielectric constant (10^9) for energies smaller than the InGaAs bandgap. In this way, we reduce the complexity of the problem while keeping the fundamental elements of the device. This approximation is used in Section 4. A more realistic approach is to introduce a DBR. Such possibility is explored in Section 5, where different combinations of materials and number of layers and periods are studied.

The report is organized as follows. As the main source on enhancement of the efficiency of the solar cell relies in the light trapping structures (LTS), we describe the two bioinspired designs in detail in Section 2. One design is inspired in the moth eye and the other on the shell of the diatoms. All the methods employed in the study are described in Section 3. The results are divided in two main sections. In Section 4 we pay special attention to the enhancement of the EOL by introducing the LTS. There we optimize the two LTSs and find that the moth eye structure provides better light absorption. Furthermore, its fabrication is simpler and has already been experimentally achieve. We also discuss the actual increase in the EOL by developing an analytical model to cope with the carrier collection probability under arbitrary generation profile across the cell. We show that the radiation damage in the interplanetary space is independent of the thickness of the layers or the LTS design but the collection probability strongly depends on the thickness.

From these two main conclusions, we proceed to look into more detail the optical approximations made so far, in particular, on the use of a SPM. In Section 5, we focus on the moth eye LTS and explore the impact of replacing the SPM by physically realizable DBRs. We then introduce the LTS in combination with a DBR, analyze the optical properties and discuss the viability of the proposal from a fabrication point of view. The two main results section complement each other covering a broad phenomenology and opening new lines of research for future implementations.

2 Bioinspired light-trapping structures

Sunlight is the primary energy source for life on earth. In some habitats and environments the solar irradiance is reduced. Species living in such an environment have developed strategies to harvest the remaining sunlight in an effective way. There is wealth of bio-inspired photonic materials with potential for solar energy harvesting. [6]. One example for this are diatoms, a pelagic microalga. Diatoms have a silica microshell (frustule) that is multifunctional: it enables the diatoms to collect the sparse sunlight and maximize their rate of photosynthesis [7] while providing it with extraordinary mechanical robustness [8]. A second example is the moth's eye (ME) structure. Moths are night insects and therefore have adapted their vision organs to

poorly illuminated environments. In particular their composed eyes resemble a periodic lattice of nano-cones. Their use as anti-reflective coatings and light-trapping structures has been exploited in solar cells to this aim [9, 10, 11, 12, 13, 14, 15].

Applying such strategies for efficient absorption of sunlight could be beneficial for solar panels on spacecraft. In the following, the characteristics of these structures and their potential to find application as a biomimetic role model for the application on spacecraft solar panels are investigated.

2.1 Moth's eye structure

The compound eyes of moth consist of corneal nipples spanned in a hexagonal lattice [16]. Inspired by this design, we studied in Refs. [14, 15] the performance of a square lattice of nanocones as anti-reflective coating in multijunction solar cells. Here we briefly summarize the main results. An schematic depiction of the structure is shown in 3(a). It is possible to distinguish the different elements of the photonic structure. The brown layer represents a GaInP substrate, the green layer corresponds to the window layer, the grey-gradient layer is a spacer and the ME is sited on top of a base layer consisting on a square lattice of cones. The geometry was optimized for a different combinations of materials to reduce the reflection losses. The results of the reflectance are reproduced in Fig. 3(b). It is always smaller than a 5% in a very broad spectral range (350 nm - 1800 nm), being remarkably smaller than that of a ZnS/MgF_2 bilayer in the short and large wavelength region. The fabrication was conducted in Ref. [15]. Many nano-lithography techniques are available, however only a few are suitable for low cost fabrication of large area devices such as solar cells. Laser interference lithography (LIL) was employed in the fabrication of ME. Mainly for its capability to uniformly pattern large areas (>1 m^2) [17, 18]. Electron beam lithography (EBL) and focused ion beam (FIB) are often used for fabricating high quality photonic crystals, but these techniques are not suitable for large area applications due to the use of finely focused beams to define the patterns point by point. Another considerable advantage of LIL is that it is a mask-less technique, in contrast with nano-imprint lithography, and therefore, it is compatible with preexisting patterns such as solar cell electrical contacts.

2.2 Diatom structure

An attempt to translate and abstract the structure of *Coscinodiscus wailesii* was made by Chen et al. [19] (see Figure 4(a)). The structure consists of three layers known as cribelum (top), cribrum (middle) and areola (bottom). To investigate the impact of a single layer, Chen et al. performed a RCWA analysis (rigorous coupled wave analysis), placing the different layer models on top of a thin-film solar cell (PTB7:PC_{71}BM layer, 50 nm thick). No enhancement peak was observed for the abstracted cribellum. This is appointed to the fact that the lattice and pore size of the cribellum layer is much smaller than the typical wavelength. In the subsequent simulations, the cribellum layer was therefore represented by a homogenize dielectric layer. However, in the case of the abstracted cribrum case, an enhancement peak is observed at a wavelength of 390 nm and a wider peak is observed for the internal plate (areola) case at a wavelength of 750 nm. In another simulation, the different layers were simulated as a stacked configuration on top of the active layer. To investigate the influence of the stacking, a simulation was performed comparing the full structure to a control case (the layers consisted of homogenized effective refractive index) and to the bare absorber. The results are reproduced in Fig. 4(b). A broadband enhancement in absorption compared to the respective control case was found. The enhancement was a factor of 1.41 (compared to 1.07 in the control case). Consequently, it can be concluded

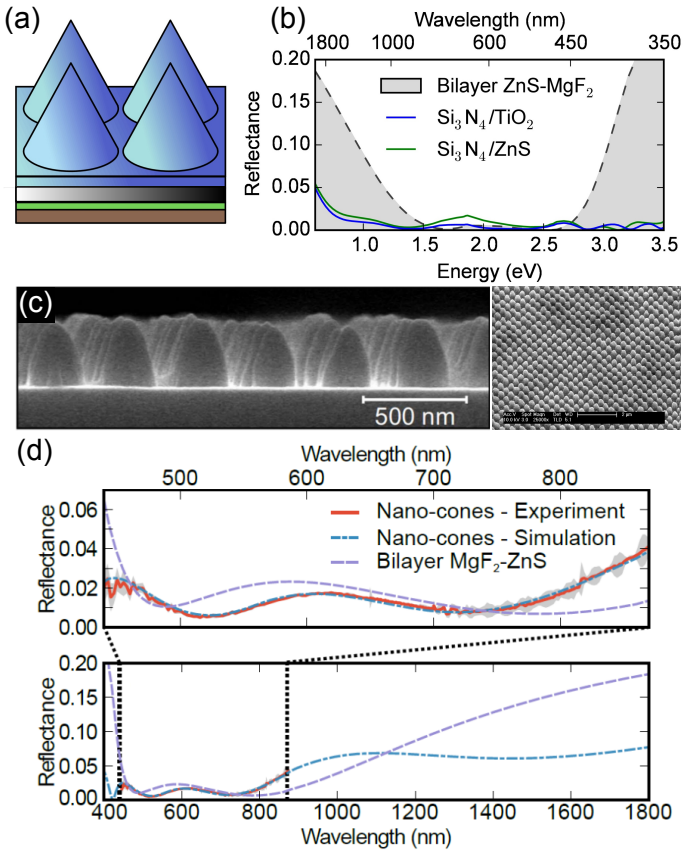

Figure 3: (a) Schematic draw of the ME structural abstraction. (b) Comparison of the reflection of the ME versus a bilayer. (c) Cross-section and planar SEM image of the ME structure fabrication. (d) Comparison of the experimental and theoretical reflection. Panels (a-b) are extracted from [14] and (c-d) from [15].

that the enhancement effect is the result of the combination of different layers. Hence it is also plausible, that a variation and combination of different layers with various pore sizes could be tailored to specific enhancement peaks.

In conclusion, the diatom structure shows a moderate enhancement of the absorption with respect to the bare and control cases. The spectrum is only analyzed in a narrow range from 400 nm to 800 nm. In addition to that the fabrication of the structure is difficult to implement as it requires the stacking of two photonic crystals of different pore size and lattice constant. In this report, we will take as starting point the diatom structure and perform an optimization of the parameters to obtain the optimal design to asses its fabrication potential.

3 Methods

3.1 Solar cell and light trapping structures

The schematic of the solar cell model is shown in Figure 5(a). For the LTS, the underlying absorbing substrates have dissimilar optical properties from the ones found in nature and the spectrum of

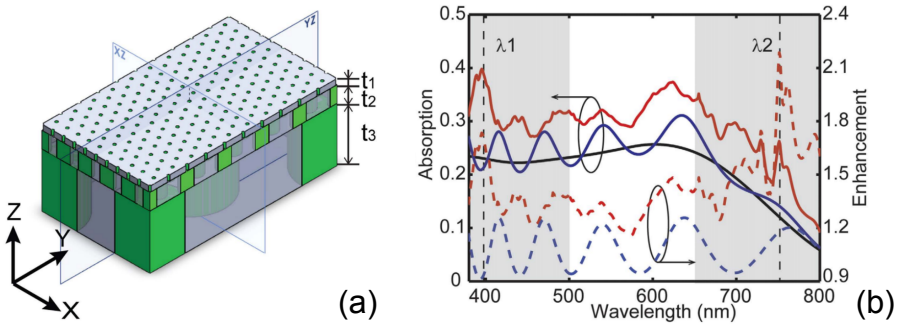

Figure 4: (a) Abstraction structure of the diatom shell consisting of three layers as described in the main text. (b) Absorption and enhancement factor of an organic absorber finished by either the diatom structure (red line), a control case (blue line) and the bare absorber (black line). Extracted from Ref. [19].

interest differs, therefore we redesigned the structures to fit the requirements of the solar cell. The geometries of the LTS were parametrized and optimized, with the goal to achieve maximum solar cell efficiency. We compare the LTS performance to a reference anti-reflective coating (ARC), which consists of two layers made of MgF_2 and ZnS with thicknesses h_1 and h_2 as shown in Figure 5(b).

The moth-eye structure is abstracted as a square lattice of cones, similar to [14, 15], with lattice constant a_m. The unit cell is shown in Figure 5(c). Each cone is described by the radius r_m and height h_m and it is placed on top of the base layer of thickness h_b, which accommodates the guided modes that participate in the light trapping. The cones and the base layer are made of TiO_2. A spacer layer of thickness h_s made of Si_3N_4 is placed between the base and the solar cell.

The diatom LTS is based on the hard cell wall (frustule) of the diatom species *Coscinodiscus wailesii* described previously. As it was mentioned before, the frustule of the *C. wailesii* is composed by three layers decorated by a hexagonal lattice of pores: the cribelum (top), cribrum (middle) and areola (bottom). The cribellum pore size is much smaller than the typical wavelength of light; simulations of the individual layers have shown that the cribelum plays a minor role in the light enhancement and can be omitted [19]. In the present study, the diatom structure consists of two layers made of TiO_2, resembling the areola and the cribrum, as shown in Figure 5(d). The unit cell of the areola layer is a rectangle with sides a_a and $\sqrt{3}a_\mathrm{a}$, perforated with holes of radii r_a. The cribrum consists of an identical unit cell, which is scaled down by an integer factor in comparison to areola $a_\mathrm{c} = a_\mathrm{a}/n_\mathrm{c}$, $n_\mathrm{c} \geq 2$, $n_\mathrm{c} \in \mathbb{N}$. We denote the radius of the holes in the cribrum layer by r_c. The two layers are displaced relative to each other by the displacement vector $r_0 \in \mathbb{R}^2$; for $r_0 = (0,0)$ the centers of all the areola holes coincide with hole centers of the cribrum. We denote the thickness of the areola and the cribum layers by h_a and h_c respectively.

3.2 BOL solar cell model

The propagation of light through the LTS structure and the solar cell was simulated using the Fourier Modal Method (FMM), also known as Scattering Matrix Method (SMM), a technique applicable to 3D layered structure with 2D periodicity. The absorption of wavelength λ at junction $i \in \{\mathrm{GaInP}, \mathrm{InGaAs}, \mathrm{Ge}\}$, $a_i(\lambda)$, is computed by solving the scattering matrix for each layer, which connects the incoming light to the Poynting flux entering and exiting the layer bounds. We use the software S^4 [20], an open-source implementation of the SMM technique. We sampled a_i at

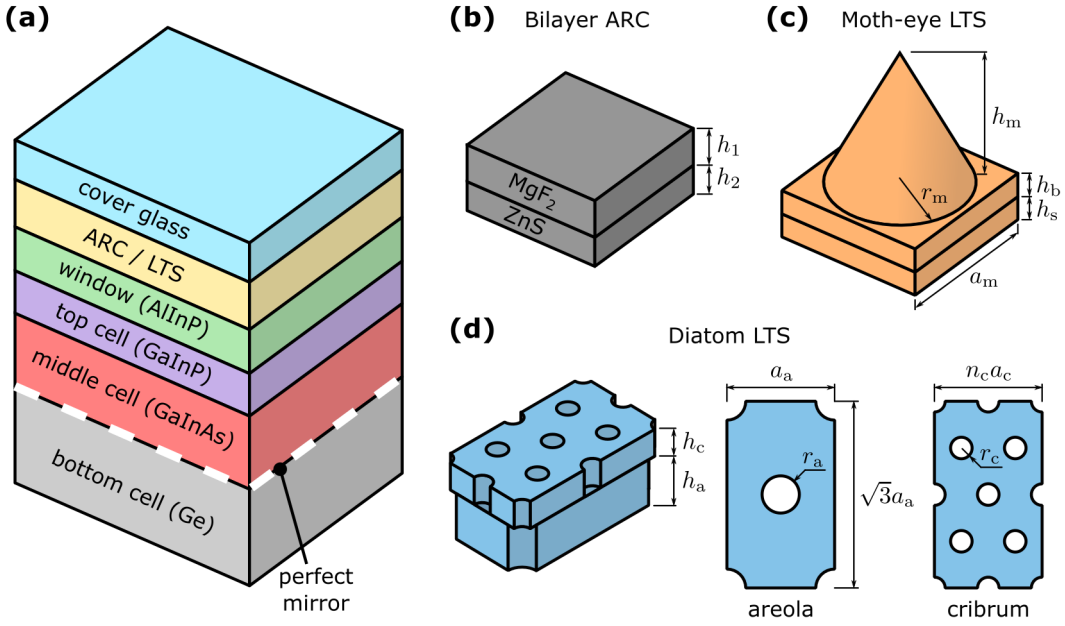

Figure 5: Schematic of the solar cell and the anti-reflective structures. (a) Layers of the triple junction solar cell. (b) Bilayer anti-reflective coating. (c) Unit cell of the moth-eye LTS. (d) Unit cell of the diatom LTS.

500 wavelengths between 350 nm and 1900 nm. For all optical simulations, we assume that the cover glass layer has a constant refractive index of $n_{\text{cover}} = 1.4$. For the rest of the materials we considered a complex wavelength-depended refractive taken from the literature (references are given in Table 1). We model the SPM by increasing the dielectric constant of the Ge substrate to a very large value ($\sim 10^9$) for photon energies >1.4 eV, i.e. the gap of the middle junction. The number of basis functions for SSM was set to 51 per unit cell; for the diatom it translates to $51 n_{\text{c}}$.

Given $a_i(\lambda)$, we estimate the efficiency of the solar cell, η, by considering an equivalent electrical circuit. Each junction is abstracted as a current source, which account for the junction photocurrent, with a radiative coupling component and an ideal diode connected in parallel. At BOL, we make the simplifying assumption of complete photocarrier collection, which is reasonable for high quality solar cells. Moreover, this definition of BOL efficiency serves as an informative figure of merit for the optical performance of the cell. Thus, the photocurrent density at junction i becomes

$$J_{\text{ph},i} = \frac{q}{hc} \int_0^{\lambda_{\text{g},i}} a_i(\lambda) \Phi(\lambda) \lambda d\lambda \tag{1}$$

where q is the charge of the electron, h is the Planck constant, c is the speed of light and $\lambda_{\text{g},i}$ is the wavelength that corresponds to the band-gap of the junction.

The spectral irradiance of the incident light, $\Phi(\lambda)$, is computed using the AM0 spectrum. The radiative coupling increases the photocurrent of the junction, if there is excess current the junction above. The increase in current of the i^{th} junction is computed using the recursion [29]

$$J_i = \begin{cases} J_{\text{ph},i} + \beta \text{ERE}(J_{i-1} - J) & J_{i-1} > J \\ J_{\text{ph},i} & \text{otherwise} \end{cases} \tag{2}$$

Table 1: Composition of materials, layer that appear in and references to their optical properties.

Material	Layer	Reference
MgF_2	bilayer ARC	[21]
ZnS	bilayer ARC	[22]
TiO_2	diatom/moth-eye LTS	[23][a]
Si_3N_4	moth-eye LTS	[24]
$Al_{0.5}In_{0.5}P$	window	[25]
$Ga_{0.51}In_{0.49}P$	top junction	[26, 27]
$Ga_{0.99}In_{0.01}As$	middle junction	[24][b]
Ge	bottom junction	[28]

[a] Properties for polycrystalline anatase.
[b] Optical properties of GaAs were used.

where J is the common current flowing through the cell, ERE is the external radiative efficiency and β is the radiative coupling parameter. No radiative coupling takes place in the first junction, namely $J_{\text{GaInP}} = J_{\text{ph,GaInP}}$. Following [30], we assume constant values for $\beta = 11$ and ERE $= 0.01$ and we compute the reverse saturation current density as

$$J_{0,i} = \gamma_i J_{\text{db},i}/\text{ERE} \tag{3}$$

$$J_{\text{db},i} = \frac{2\pi q (kT)^3}{h^3 c^2}\left[\left(\frac{E_{\text{g},i}}{kT}+1\right)^2+1\right] e^{-E_{\text{g},i}/kT} \tag{4}$$

where k is the Boltzmann constant, T the absolute temperature of interest and $E_{\text{g},i}$ is the band gap at the i^{th} junction. The coefficient $\gamma_i = 1+\beta$ for junctions with the ideal SPM (top and middle in the present study) and $\gamma_i = 1$ for the rest. The cell voltage is the sum of the voltage of each junction

$$V = -RJ + \sum_i \frac{kT}{q}\ln\left(\frac{J_i - J}{J_{0,i}}+1\right) \tag{5}$$

with the series resistor $R = 4\times 10^{-5}\,\Omega\,\text{m}^2$ lumping the contribution of all internal losses. We determine the maximum power numerically, $P_{\max} = \max(VJ)$ and compute the efficiency as:

$$\eta = \frac{P_{\max}}{\int \Phi d\lambda} \tag{6}$$

3.3 EOL solar cell model

To connect the radiation exposure to the cell efficiency, we expanded the solar cell model to account for defect-induced changes in the semiconductor properties. Specifically, we assume that the introduction of defects in the semiconductor lattice decreases the minority carrier lifetime from the initial value of $\tau_{0,a}$ to the value τ_a after irradiation. The subscript a can refer either to electrons, n, or holes, p, depending on the type of doping. The relation of τ_a with the radiation exposure is described in detail in the subsequent Section 3.4. Moreover, we neglect the radiation damage on the top and bottom junctions because the deterioration in solar cell performance is dominated by the degradation of the middle junction [31, 32, 33]. For the top and middle junctions we assume complete photocarrier collection.

The effect of the reduced lifetime in the solar cell efficiency is accounted for by expanding the BOL model to include 1D diffusion dynamics. Appendix A describes the 1D diffusion model and proposes an analytical solution. Two main adjustments are introduced in comparison to the complete photon collection assumption. First, the photocurrent is limited a τ_a-depedent collection probability, P_c, which modifies Eq. (1) as

$$J_{\text{ph,InGaAs}} = \frac{q}{hc} \int_0^{h_{\text{InGaAs}}} \int_0^{\lambda_g} P_c(x) a(\lambda, x) \Phi\text{-}(\lambda) \lambda d\lambda dx \tag{7}$$

where x is the depth in the junction measured from the top and h_{InGaAs} is the thickness of the middle junction. We note that the absorption coefficient is a function of both λ and x in Eq. (7). Second, the junction saturation current increases due to the diffusion dynamics by the term J_{d0} as

$$J_{0,\text{InGaAs}} = \gamma J_{\text{db,InGaAs}} / \text{ERE} + J_{d0}. \tag{8}$$

The calculation of the radiative coupling is performed as before, with the difference that $J_{\text{ph,InGaAs}}$ is calculated using Eq. (7).

For the undamaged cell, we assume that $\tau_{0,a}$ is dominated by the radiation recombination lifetime and depends on the dopant concentrations as $\tau_{0,n} = (BN_a)^{-1}$ and $\tau_{0,p} = (BN_d)^{-1}$, with N_a and N_d being the acceptor and donors concentrations respectively. The previous relations have been derived under the assumption that the majority carrier concentrations are approximately equal to the respective dopant concentrations. For the simulations, we used value of GaAs $B = 2 \times 10^{-10}\,\text{cm}^3\,\text{s}^{-1}$ for the recombination probability [32].

3.4 Radiation damage modeling

The impact of radiation on τ_a was assessed using Monte Carlo simulations. High energy particle lose energy as they traverse through a material that falls into one of two categories [34, 35]: a) electronic energy loss, which includes interactions of the projectile with the bound electrons of the medium and b) nuclear energy loss, which accounts for the collisions between the projectile and the atoms of the medium. Semiconductor degradation is connected to a portion of the nuclear energy loss referred to as the non-ionizing energy loss (NIEL). The NIEL deposited energy disturbs the nuclei off the semiconductor lattice, leading to the appearance of atomic displacements. Specifically, the energy deposited on atomic displacement per unit mass of the semiconductor, termed the damage dose D_d, has been directly connected to the Frenkel pairs (FP, vacancy-interstitial pairs) density [36, 34].

The damage dose induced by a radiation source with spectral fluence ϕ (number of particles per area per energy) is equal to

$$D_d = \int \phi(E_p) \frac{dE_{de}(E_p)}{d\chi} dE_p \tag{9}$$

where E_p is the energy of the incoming particle and $dE_{de}/d\chi$ is the displacement mass stopping power, namely the energy deposited on atomic displacements per unit path length normalized by the material density. Semiconductor atoms recoil with energy E_r after interaction with the particles and permanent defects occur if E_r is greater than a material dependent displacement threshold energy E_d. Even if $E_r \geq E_d$, only part of E_r contributes to stable defect formation, captured by the Lindhard partition $L(E_r)$, whereas the rest is dissipated as lattice vibrations [37, 38]. Hence, the mass stopping power for all interaction is given as a function of E_p as

$$\frac{dE_{de}(E_p)}{d\chi} = \frac{N_A}{A} \sum_k \int_{E_d}^{E_M} E_r L(E_r) \frac{d\sigma_k(E_p, E_r)}{dE_r} dE_r \tag{10}$$

where N_A is the Avogadro number, A is the atomic weight of the medium, $d\sigma_k/dE_r$ is the differential cross section of the k-th reaction and E_M is the maximum recoil energy achievable by E_p. The summation is taken over all possible reactions between the projectile and the semiconductor atoms. For protons and electrons interactions with the lattice atoms occur through Coulomb scattering. Additionally, for protons with energies above ∼10 MeV, nuclear elastic and inelastic reactions has to be taken into account [39]. Eq. (10) is valid for simple substances, whereas for compound materials Bragg's rule applies; the mass stopping power is calculated as the sum of the mass stopping power of each material weighted by its mass fraction [31].

We employed the Geant4 software [40] to assess the impact of thinning the middle junction on D_d (see Appendix B for simulation details). During the simulations, we track particle path and record E_r of primary knock-on atoms (PKA, atoms that were displaced due to interaction with the energetic particles) in the middle junction. We set $E_d = 21$ eV, value that has been proposed for GaAs [31, 33], and use the formulation in [37] for $L(E_r)$. We approximate Eq. (9) as

$$D_d = \frac{\phi_0}{\phi m_s} \sum_{n=1}^{N} E_{r,n} L(E_{r,n}) \tag{11}$$

where n is the event index, N is the total number of recorded PKA events, m_s is the mass of the middle junction and ϕ_0 is a reference fluence. The Frenkel pair concentration is computed by means of the modified Kinchin–Pease formula [34]

$$\mathrm{FP} \sim \frac{D_d \rho_s}{E_d} \tag{12}$$

where ρ_s is the density of the middle junction material. We treat quantities that computed from the Monte Carlo simulations as random variables and report the mean values with the 99 % confidence interval (CI). For D_d, the mean value is computed from Eq. (11) and the variance from

$$\sigma_D^2 = \left(\frac{\phi_0}{\phi m_s}\right)^2 \sum_{m=1}^{M} \left[E_{r,m} L(E_{r,m})\right]^2 . \tag{13}$$

The distribution of D_d is assumed normal due to large number of recorded event, similar to [41].

The FP density is connected to τ_a as follows: the increase in the inverse of the lifetime has been shown to be proportional to FP [34], and as a consequence of Eq. (12) is also proportional to D_d. Therefore, after irradiation

$$\frac{1}{\tau_a} = \frac{1}{\tau_{0,a}} + K_a D_d \tag{14}$$

where K_a is the damage coefficient. We note that Eq. (14) is equivalent to the commonly used formula that connects the increase in the inverse of the lifetime to ϕ [42, 32].

3.5 Geometry optimization

For optimizing the LTS geometries, we are interested in attaining the maximum efficiency, η, while keeping the thickness of the middle junction, h_{InGaAs}, minimum. These requirements form a multi-objective optimization problem:

$$\begin{aligned} \min_{z_p} \quad & (-\eta, h_{InGaAs}) \\ \text{s.t.} \quad & z_p \in Z \end{aligned} \tag{15}$$

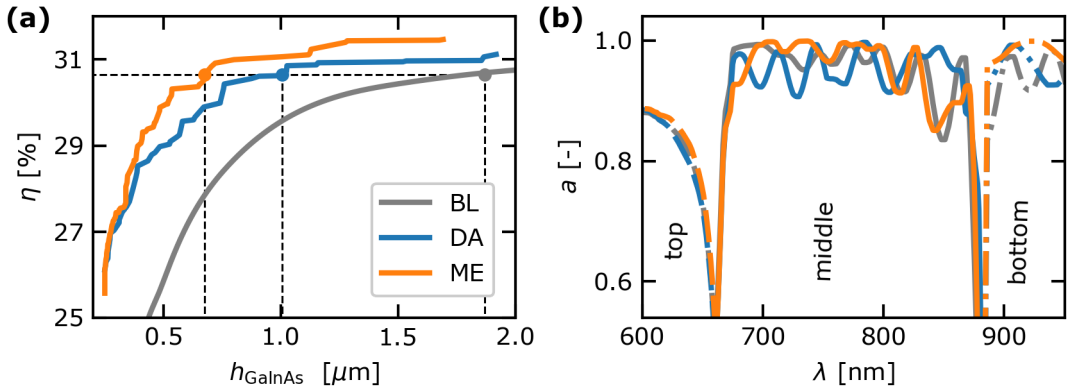

Figure 6: Optimization results for the LTS. (a) Comparison of the BOL efficiency between the LTS and the BL ARC. (b) Detail of the absorption of the middle junction per wavelength for solar cells with the BL and the LTS with equal BOL efficiency. The depicted absorption profiles correspond to the points in panel (a).

where z_p is a vector holding the parameters of the LTS geometry. The set of allowable solutions, Z, incorporates the constraints on the parameters that encode meaningful solutions. The solution to Eq. (15) is composed by the set of points, referred to as the Pareto front. Any point on the Pareto front cannot be further improved without sacrificing at least one of the objectives.

We obtain the Pareto front using the software package Pygmo [43]. We employed the evolutionary algorithm NSGA-II, which imitates the process of natural selection. Every distinct LTS geometry is seen as an "individual", which described by its "chromosome" z_p. An initial population satisfying Z is selected randomly. At each step (generation), new individuals are created by crossing (mating) and mutation operations. Each new individual is assigned a fitness score, in our case the tuple $(-\eta, h_{InGaAs})$, and the next population is selected by taken the fitness score into account (survival of the fittest). Different populations can be evolve simultaneously and exchanging individuals during their evolution (island with migration model). The results for the diatom LTS obtained a single populations of 52 individuals evolved for at least 270 generations. The moth-eye geometry was optimized in 4 fully connected islands of 24 individuals each for 50 generations.

4 Results on radiation damage

4.1 Optimized LTS

Figure 6(a) compares the Pareto fronts for the diatom with $n_c = 2$ and moth-eye LTS to the bilayer ARC, as resulted from the optimization procedure. For the bilayer ARC, the optimal structure was determined to have a constant $h_1 = 91.5\,\text{nm}$ and h_2 decreasing from 59.3 nm to 53.7 nm as the thickness of the middle junction increases. Both LTS achieve higher η values for the whole range of h_{InGaAs} in comparison to the bilayer ARC, with the highest improvement occurring as the middle junction becomes thinner. Substituting the bilayer ARC with the LTS allows to reduce the thickness of the middle junction from 1.87 µm for the reference design down to 1.00 µm or 0.68 µm for the diatom and the moth-eye LTS, respectively, without sacrificing the BOL efficiency. The absorption at the wavelengths of interest for the middle junction is contrasted in Fig. 6(b)

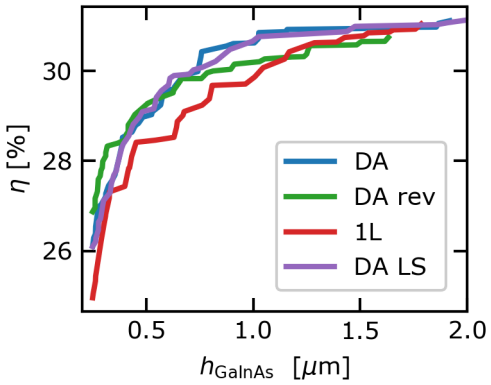

Figure 7: Optimal solar cell efficiency for different configurations of the diatom LTS. Four configurations are shown: normal layer ordering (DA), reversed ordering with the areola on top of the cribrum layer (DA rev), single layers with hexagonal pores (1L) and normal layer ordering with n_c as a optimization parameter (DA LS).

for the bilayer ARC and the LTS with equal BOL $\eta \approx 30.64\,\%$. Setting the LTS and the reference structure at a equivalent BOL efficiency, makes for a reasonable and informative way to compare the radiation hardness of the different designs.

We present the geometrical parameters of the optimized structures in Appendix C. The diatom structure though is composed by two photonic crystals of different pore size and lattice constant, making a more complicated structure from a fabrication point of view. The set of parameters introduced in Section 3.1 do not encode all the possibilities and do not shed light on the importance of the cribrum layer. Thus, we repeated the optimizations for two additional configurations: a reversed ordering diatom, with the areola placed on top of the cribrum and a single dielectric layer with pores in a hexagonal lattice. We describe the latter configuration using the geometrical parameters of the areola, e.g. we use a_a for the lattice constant. Additionally, we performed the optimization with the normal ordering for the diatom including $n_c \in [2, 5]$ as an optimization parameter. The achieved maximum efficiency for the aforementioned configurations is shown in Fig. 7. The normal ordering is the most successful for wide range of h_{InGaAs}. Only for very thin junctions, below 0.4 µm, the reversed configuration is able to achieve the highest efficiencies. Optimizations with n_c as a free parameter did not achieve substantially improved results in comparison to fixing $n_c = 2$. The single layer with pores attained the lowest η for the vast range of h_{InGaAs} or comparable for thick junctions.

4.2 Radiation induced damage

The LTS enable a substantial decrease in the thickness of the middle junction. To quantify the potential improvement in radiation hardness, we first assess the impact of thinning of the junction on D_d and consequently on the defect density. The relation between D_d and h_{InGaAs} allows to determine the decrease in the minority carrier lifetime for different cells designs at the same radiation exposure. To isolate the effects coming from the junction thinning alone, we simulated the solar cell with the bilayer ARC without the protective cover glass for middle junction thickness from 0.2 µm to 2.0 µm. The material and thickness of the rest of the layers is the same as the one used for the optical simulations. The thickness of the bottom junction was fixed to 148 µm. Figure 8(a) and (b) plots D_d inflicted on the middle junction for monoenergetic electrons of 1 MeV and

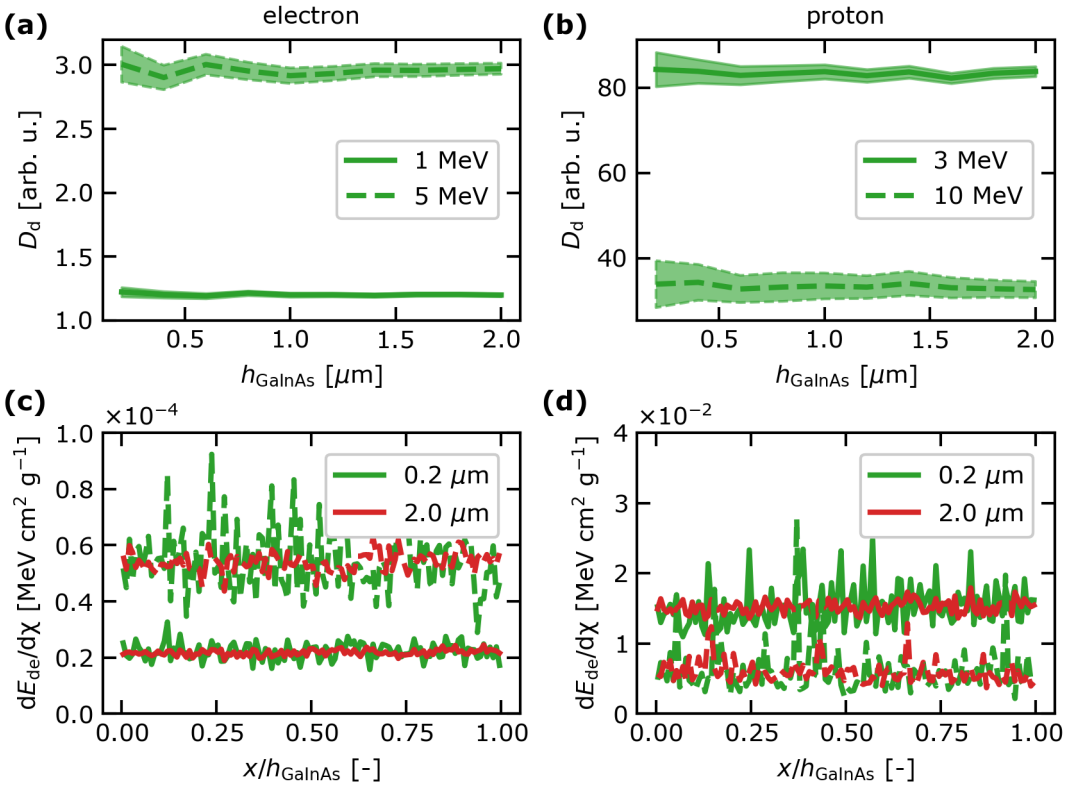

Figure 8: Radiation damage for different thicknesses of the middle junction. (a) Damage dose in arbitrary units deposited on the middle junction of a solar cell for incident electrons of 1 MeV and 5 MeV. The middle junction thickness varies from 0.2 µm to 2.0 µm, while all the other layers are keep constant. (b) Same as panel (a) for proton of 3 MeV and 10 MeV. (c) Mass stopping power as measured along the normalized junction depth. The presented values correspond to the two extreme thickness of panel (a). CI has been omitted for the shake of clarity. (d) Same as panel (c) for proton irradiation.

Table 2: Comparison of D_d [10^9 MeV g^{-1}] between solar cells with the LTS and the bilayer ARC. Results for one year in orbit with ϕ_0 equal to the total particle fluence.

orbit	BL	DA	ME
LEO	7.39 ± 2.09	6.63 ± 1.31	6.62 ± 1.57
HEO	1261 ± 61	1338 ± 90	1257 ± 101
GEO	29.9 ± 7.3	32.8 ± 11.9	28.0 ± 8.2

5 MeV, and protons of 3 MeV and 10 MeV at normal incidence; D_d depends on the energy and the type of the incident particle but not on the thickness of the middle junction. The independence of D_d from the junction thickness implies that for a given particle and energy, $dE_{de}/d\chi$ remains almost constant as the particle traverses the middle junction. This is confirmed by the recorded values of $dE_{de}/d\chi$ for the aforementioned cases, which are shown in Fig. 8(c) and (d) for the two extreme cases of middle junction thickness.

Still, the dissimilar materials and thicknesses of the layers between the ARC and the LTS may affect the induced defect density. We repeat the simulations for the cells with the optimized LTS and reference ARC with an equivalent BOL efficiency, which we described in Section 4.1. We selected a representative space radiation environment, composed of electrons and protons meeting the solar cell at angles ranging from 0° to 90°. Three different orbits were considered: a low-earth orbit (LEO), a highly elliptical orbit (HEO) and a geostationary orbit (GEO). Appendix B details the energy spectra the cells encounter in these orbits. All cells were simulated with a protective cover glass of 100 µm. Table 2 compares the D_d for the three solar cell designs, verifying that the solar cell degradation is connected to the radiation environment and not to the junction thickness or the LTS.

4.3 EOL efficiency analysis

The radiation induced defect density on the middle junction is independent from the junction thickness and the anti-reflective coating or the LTS, as discussed in Section 4.2. Therefore, the deterioration in cell efficiency for different combinations of junction thickness and LTS can be compared at a given radiation exposure by computing η at equal values of τ_a.

For the reference middle junction design, we assume an emitter with width $x_W = 0.5\,\mu$m and we set the doping concentrations for acceptors at $N_a = 5 \times 10^{16}\,$cm^{-3} and for donors at $N_d = 2 \times 10^{17}\,$cm^{-3}. We simulate cells with n and p-doped emitters. We connect τ_a to D_d using the values $K_p = 0.04\,$g MeV^{-1} s^{-1} and $K_n = 0.23\,$g MeV^{-1} s^{-1}, taken from [42]. Figure 9(a) compares the cell degradation at different radiation exposures for the solar cell designs with equivalent BOL efficiencies from Section 4.1. The solid lines refer to p-doped emitter and the dashed lines to n-doped emitter. We included the experimental values for the 3G30C cell [1] for comparison. The experimental η values for 3G30C cell are reported for 1 MeV electron irradiation and the same applies for K_p and K_n: the conversion to D_d is performed with the coefficient $2.246 \times 10^{-5}\,$MeV cm^{-2} g^{-1} computed in Section 4.2. Moreover, we plot the mean collection probability over the junction width

$$P_t = \frac{1}{h_{InGaAs}} \int_0^{h_{InGaAs}} P_c(x)dx \tag{16}$$

in Fig. 9(b).

The LTS equipped cells demonstrate higher radiation hardness, with η being higher for all values of D_d in comparison to the ARC design. For the p-doped emitter, the thinner the junction

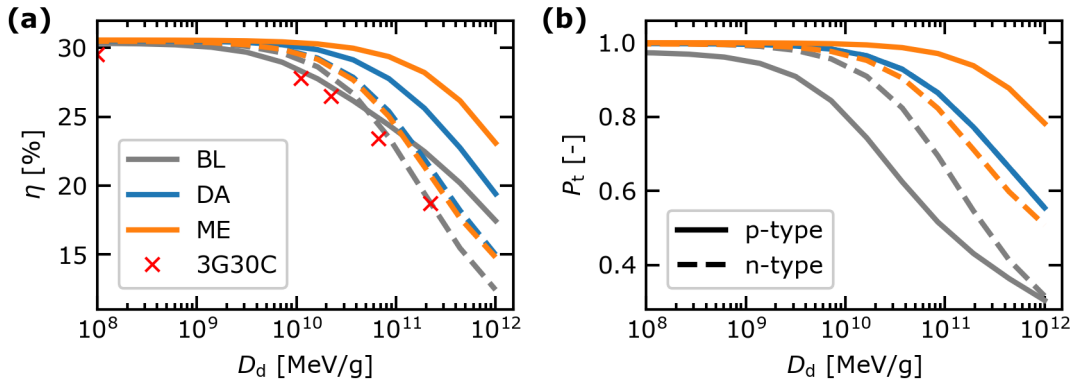

Figure 9: Comparison of EOL efficiency at different D_{d}. (a) Efficiency deterioration for various levels of D_{d} for cells with equivalent BOL efficiencies (BL for bilayer ARC, DA for diatom LTS, ME for moth-eye LTS). Values for the 3G30C cell from [1] are included for comparison. Solid and dashed lines distinguish p and n-doped junctions respectively. (b) Mean collection probability over the junction width for the same cases as panel (a). Diatom P_{t} curve for the p and n-doped emitters overlaps.

the less the cell is affected by radiation, with the EOL efficiency for the moth-eye equipped cell being almost 6.0 % higher than the reference cell at high D_{d}. When the emitter is n-doped, all designs showed faster degradation, partially reflecting the smaller value of $\tau_{0,\mathrm{p}}$ in comparison to $\tau_{0,\mathrm{n}}$. In this case, the cell with the diatom LTS showed marginally the slowest degradation, with a 2.7 % EOL η difference to the reference cell. The mean collection probability captures adequately the trends in η for similar cell designs. Yet, for the diatom LTS cell where the symmetry of the design—the total junction width being 1.0 µm and the emitter width being 0.5 µm—results in equal values for P_{t} for both the n and p emitters, the corresponding efficiency degradation profiles are quite different. This highlights the important of maximizing P_{c} close to the incident of the light, where the absorption is the highest. The computed η curves show a similar trend as the experimental results of the 3G30C cell, without any fitting of the parameters. Moreover, it is common to use the expression

$$RF_{\mathrm{j}} = 1 - C \log_{10}\left(1 + \frac{D_{\mathrm{d}}}{D_{\mathrm{x}}}\right) \tag{17}$$

to describe the degradation of the cells [44, 45, 31, 33], where $RF_{\mathrm{j}} = \eta\eta_0^{-1}$ is the efficiency remaining factor, η_0 is the BOL efficiency and C, D_{x} are fitting parameters. We examine the capacity of Eq. (17) to represent the simulated curves from Figure 9(a). The fittings are indistinguishable from the data, with the smallest coefficient of determination being $R^2 > 0.997$, illustrating the validity of our model.

The results indicate that several parameters influence the solar cell radiation hardness. To gain a better understanding, we investigated how the emitter width and the doping density may affect the EOL efficiency at a constant $D_{\mathrm{d}} = 10^{11}\,\mathrm{MeV\,g^{-1}}$. The assumption of complete photon collection at BOL is not valid in this case, especially for high doping densities where $\tau_{0,a}$ may significantly decrease. Accordingly, we report the RF_{j}, with η_0 calculated at $D_{\mathrm{d}} = 0$. First, we calculated RF_{j} for values of the emitter width ranging from $x_{\mathrm{W}} = 0.10\,\mu\mathrm{m}$ to $x_{\mathrm{W}} = h_{\mathrm{InGaAs}} - 0.10\,\mu\mathrm{m}$. The acceptor and donor concentrations are kept as in the reference junction. Figure 10(a) plots the remaining factor for the LTS and the reference cell designs at various values of x_{W}. The p-type emitter

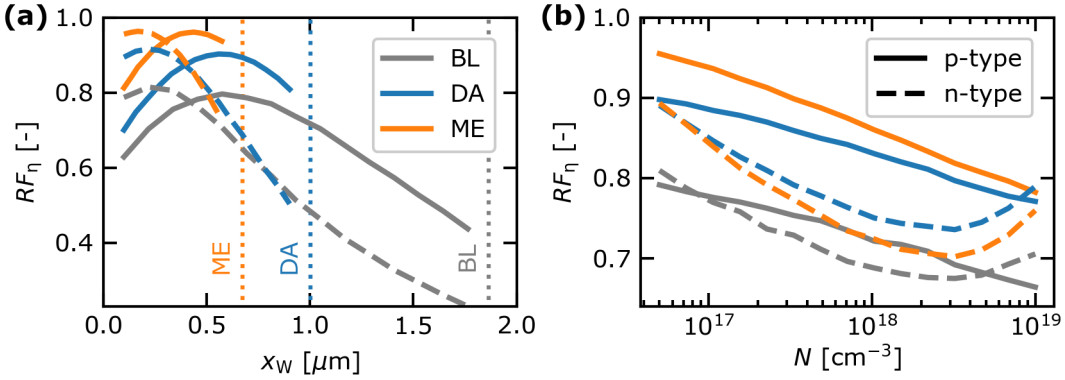

Figure 10: Comparison of efficiency remaining factor for different emitter parameters at $D_d = 10^{11}$ MeV g^{-1}. (a) Efficiency remaining factor versus emitter width for cells with equivalent BOL efficiencies (BL for bilayer ARC, DA for diatom LTS). Solid and dashed lines distinguish p and n-doped junctions respectively. (b) Efficiency remaining factor versus emitter concentration.

shows a maximum between 0.42 µm to 0.57 µm for all designs. The moth-eye LTS combined with the thinner junction exhibits the highest radiation hardness. The maximum η for the n-doped emitter lies close to 0.21 µm for all designs. As the emitter becomes deeper, the efficiency falls sharply. We note that the η_0 values remain mostly close to the ones of perfect collection; only the bilayer reference cell showed a reduction in η_0 by 0.6 % for the p-doped and 1.7 % for the n-doped deepest emitter. Further, we simulated the irradiated cell for emitter doping concentration from 5×10^{16} cm^{-3} to 10^{19} cm^{-3}, with base concentration and emitter width as in the reference junction. The results are shown in Fig. 10(b).

In general, the dopant concentration has a lesser impact on RF_j with the lowest concentration exhibiting the highest hardness. As the dopant concentration increase, RF_j for p-type emitter monotonically declines whereas it exhibits a minimum at around 3×10^{18} cm^{-3} for the n-type emitter. Interestingly, the cell with diatom LTS demonstrated the highest η for all values of n-doped emitter concentrations. For the p-type emitter, η_0 is almost constant for the investigated N_d range. Significant decline in η_0 was recorded for the n-type emitter for $Nd > 5 \times 10^{17}$ cm^{-3}, with values dipping up to 8.3 % for the bilayer ARC cell at the highest concentration.

4.4 Discussion on radiation damage effects

The LTS, inspired by the moth-eye and the diatom patterns, increase the efficiency of solar cell in comparison to the commonly industrially used bilayer ARC, especially for cells with thin middle junction.

The bilayer ARC improves light absorption by decreasing the reflectance of the front surface, minimizing the optical losses. The LTS further boost the efficiency by diffracting light, which in combination with the SPM couples at the guided modes of the middle junction. The diatom LTS incorporates two photonic crystals, opening more diffraction orders at two separate wavelengths. The higher enhancement in η observed for the normal and the reversed diatom configurations in comparison to the single perforated layer can be attributed to this fact.

These results reflect that the two-fold diffraction introduced by two stacked photonic crystals is indeed very beneficial to enhance the efficiency of the solar cell above the single layer case. Chen et al. [19] showed for an ultra-thin (50 nm) organic absorber that the total enhancement is the

combination of each individual photonic crystal contribution, which agrees with our results. In the reverse order, the large lattice constant a_a is facing the front medium which might introduce reflection losses. This can explain the reduction in efficiency for the thick layers (see Fig. 7), where diffraction is not as important as the anti-reflection mechanism. For thin InGaAs, the efficiency of both orderings are similar, being even higher for the thinnest cases under study. This again is in line with the results of Ref. [19], as the authors show a similar enhancement for the reversed order for the ultra-thin absorber. Still, the enhancement due to the diatom LTS is comparable to the moth-eye structure only for h_{InGaAs} smaller than approximately 0.4 µm. The tapered surface of the cones has a higher capacity for diffracting light.

Aside for the solar cell performance, adoption of light trapping technologies is also governed by ease of manufacturing. The bilayer ARC, composed of two simple layers, is definitely the simplest to manufacture. Progress in manufacturing processes have made large scale production of 3D structures possible. The moth-eye cone pattern has been transferred to Si_3N_4 by laser interference lithography [15], a technique capable to uniformly pattern large areas. Moreover, the nanocone arrays has been manufactured out of Si [46], TiO_2 [47, 48] and glass [49] using plasma and dry etching. The double photonic crystal arrangement of the diatom structure makes its assembly a challenging task. Precise porous hexagonal array, resembling the single diatom layer, have been fabricated using the photochemical etching technique [50], but bonding of the two layers is necessary to complete the diatom structure. A fabrication process is explained in [51] for a square lattice, although the authors recognize the challenge it represents. The implementation of the SPM posses similar issues. A selective reflective layer can be realized as a distributed Bragg reflector. For the DBR to achieve the necessary wavelength bandwidth, the use of materials with high refractive index contrast is unavoidable. Additionally, the extinction coefficient of the DBR material should be as low as possible to avoid any parasitic losses. These requirements may be only attainable for a four terminal solar cell designs, a point that needs further investigation. An alternative could be the use of an interstitial diffraction grating [52], although this also posses several difficulties.

According to our simulations, the radiation damage sustained by thin cell junctions in space is mainly governed by the radiation environment. Taking into account the energy deposition mechanism, this is a reasonable observation. The energy of the incident particle dictates the rate of energy loss along the trajectory through a given material.

For highly energetic particles the total energy deposit is small compared to the initial energy, since the solar cell structure is relative thin. Therefore, the energy of the particle remains almost constant along its path and so does the deposited energy per unit path length, resulting in an almost constant D_d. There are cases where localized energy deposit may take place in the semiconductor material, like for low energy protons that can be stopped inside the junction with a Bragg peak produced at the end of the track. The continuous energy spectrum of the typical space environment and the wide range of incident angles would diminish any localized effect. This conclusion of approximately uniform damage distribution throughout the cell active region is in agreement with [53], where omnidirectional proton irradiation was analyzed.

Thinning of the middle junction provides a compelling way to increase the radiation hardness of multi-junction solar cells. The junction thickness is however just one of the parameters that determines the sensitivity of the cell efficiency to the introduction of defects. Reduction in junction thickness should be accompanied by systematic tuning of the cell emitter width and doping concentration, to extort the maximum possible improvement with respect to cell radiation hardness. The emitter width has previously been connected to the radiation hardness of solar cells, with shallow emitters exhibiting slower degradation [42]. This fact is in accordance to our results and more prominent for the simulated n-doped emitter cells. Lowering the doping concentration

has a positive effect on radiation hardness as suggested by the recorded efficiency remaining factors; simulations performed by [32] show the exact same trend, whereas in [54] medium to high emitter doping densities achieved the highest power remaining factor.

From the mission design point of view, the thickness of the protective cover glass has been the single design parameter to control the radiation degradation for space solar cells, an approach that has been extensively discussed previously [44, 55]. The cover glass thickness affects the sustained damage by altering the energy spectrum perceived by the solar cell material through shielding. Reducing the sensitivity of the cells to radiation is a complementary approach to shielding and both methods can be applied simultaneously. This can results in reduction of the array weight, either from reducing the protective glass thickness or the number of panels needed to achieve the EOL power requirements.

5 Results on the moth eye structure with interstitial mirror

Two of the main conclusions derived from the study of Section 4 are the convenience of reducing the thickness of the middle junction to enhanced the EOL and of using the ME inspired LTS vs. the DA one.

This Section brings further the optical part of the solar cell model developed in the previous Section by replacing the selective perfect mirror by a realistic distributed-Bragg reflector (DBR). The role of the DBR is analyzed using a bilayer-ARC and, later, with the ME LTS.

5.1 Efficiency of bilayer-ARC an interstitial selective mirror

We are interested in finding a physical system which can reflect the light of energy greater than the $In_{0.01}Ga_{0.99}As$ bandgap. This light would be absorbed in the top two junctions instead of being transmitted into the Ge substrate. At the same time, photons with energy lower that the bandgap need to be transmitted to let the bottom junction contribute to the photocurrent.

The simplest selective mirror that can be introduced in the tandem cell is a distributed Bragg reflector. It consists of a bilayer structure repeated N times. The reflection is the result of destructive interference in the back propagating direction when the optical path length equals a quarter of a predefined wavelength, i.e. $n_{\mathrm{L}}d_{\mathrm{L}} = n_{\mathrm{H}}d_{\mathrm{H}} = \lambda_0/4$, where n refers to the refractive index, d to the layer thickness and L(H) labels the low and high refractive index layers. The reflectance at λ_0 is $R = \left[\left(n_{\mathrm{L}}^{2N} - n_{\mathrm{H}}^{2N}\right) / \left(n_{\mathrm{L}}^{2N} + n_{\mathrm{H}}^{2N}\right)\right]^2$ and the spectral width can be approximated by $\Delta\lambda/\lambda_0 = 4/\pi \arcsin\left[|n_{\mathrm{L}} - n_{\mathrm{H}}|/(n_{\mathrm{L}} + n_{\mathrm{H}})\right]$, hence, the refractive index contrast would determine the spectral width of the mirror and the number of layers the sharpness of the window. [56] From the epitaxial point of view, the material comprising the DBR used in monolythic solar cells are $Al_xGa_{1-x}As$, being the Al concentration the parameter fixing the refractive index contrast. The highest value is found for the two binaries AlAs/GaAs, being $n_{\mathrm{H}} - n_{\mathrm{l}} = 0.6$ at $\lambda_0 = 875$ nm, which results in a spectral window of ≈ 100 nm. However, the absorption spectrum of the middle junction spans over 233 nm, meaning that just a single DBR is not sufficient. Increasing the reflectance window, or the photonic bandgap (PBG), is an extensively explored problem in the literature. The first immediate approach is combining DBRs of different periods but equal filling factor to overlap the high reflectance regions. [57] A less direct approach it to introduce disorder in a larger arrangement to expand the PBG [58].

For the sake of simplicity we will consider here a stack of DBRs. Four systems are analyzed to illustrate the effect of the interstitial mirror: i) no DBR case (NDBR), ii) selective perfect mirror (SPM), iii) AlAs/$Al_{0.315}Ga_{0.685}As$ DBR (LDBR) and v) a high-index contrast single DBR made

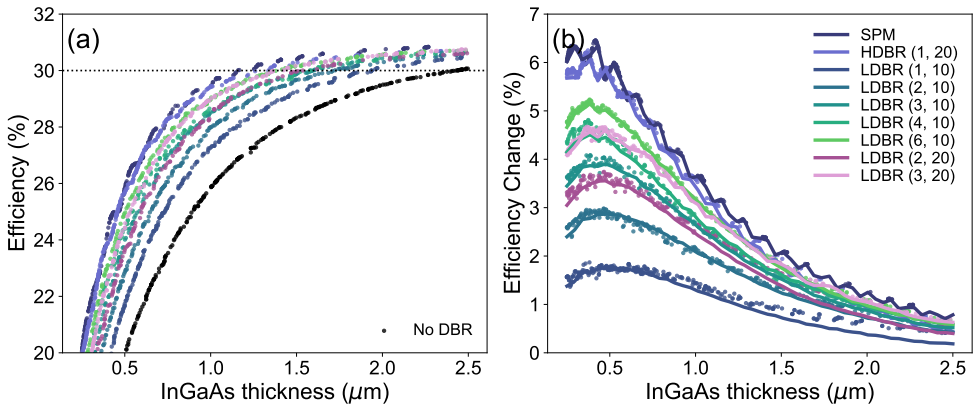

Figure 11: (a) Total efficiency of the tandem solar cells as a function of the InGaAs thickness with a bilayer ARC. Each point is the solution of an optimization. Black dots correspond to the solar cell without interstitial mirror (NDBR). LDBR is indicated through the number of stacks and layers in each stack (M,N). (b) Increase in efficiency with respect to the NDBR case. The lines show the dependence on h_{InGaAs} of the optimal solution at the position of the maximum ($h_{\text{InGaAs}} \approx 430$ nm.)

of SiO_2/TiO_2 (HDBR). To show the effect of stacking different DBRs we have explored different combinations of the LDBR system labeled as (M, N), being M the number of stacks of N pairs. The dependence of the efficiency on the InGaAs thickness (h_{InGaAs}) is shown in Figure 11(a). The different dots represent the optimal solution found by the genetic algorithm at each value of h_{InGaAs}. The family of points is known as the Pareto-optimal front (see Section 3.5), representing the best compromise between the maximization of the efficiency and minimization of h_{InGaAs}. The black dots are the solution without mirror (NDBR). Just by inserting a single LDBR [case (1,10)] we can observe a remarkable enhancement in the efficiency. To show the improvement in a clearer way, we show in Figure 11(b) the efficiency of each calculation with respect to the NDBR case. The efficiency increases monotonically as more DBR stacks are added, i.e. increasing M. For the same number of layers $M \times N$, cases (2, 20):(1, 40) and (3, 20):(6, 10) we observe that their performance is very similar with a slight enhancement for higher M. The maximum expected efficiency is represented by the SPM system, where all the light that could be absorbed in the first two junctions is reflected without parasitic losses instead of being transmitted to the bottom junction. The arsenide-based DBR approaches this limit only in the case of large h_{InGaAs} (larger than 1.5 µm). In contrast, the HDBR can easily reach that limit with just one stack of 20 layers.

The lines in Fig. 11(b) show the evolution for a fixed value of the ARC and DBR thickness of the comprising layers. We take those values from the optimal solution an $h_{\text{InGaAs}} = 430$ nm. About this thickness, the efficiency change shows a maximum. In general, the lines overlap quite precisely over the dots, showing that a single set of parameters can be used independently of h_{InGaAs}. The main difference is shown by the LDBR (1, 10) case, given that the spectral width of the mirror is very narrow and hence sensitive to its spectral position. The values taken by the different parameters are moved to the Appendix D.

To show the effect of the DBR on the optical properties, we show in Figure 12 the absorption profile in the middle and bottom junctions. The absorption in the bottom junction overlaps with that of the middle junction, although the lines can be easily discriminated due to their relative value. The former are located at the bottom part and the latter in the upper part. The dark shaded areas show the results for the SPM and HDBR structures. In both cases the absorption in

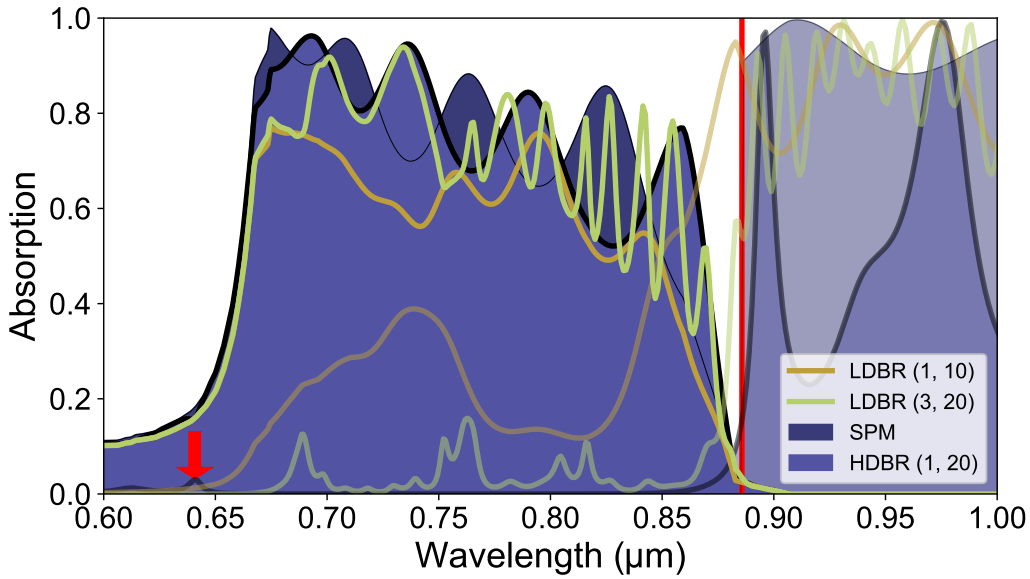

Figure 12: Absorption in InGaAs and Ge junctions for four DBR structures for $h_{\mathrm{InGaAs}} = 500$ nm. The vertical red line indicates the InGaAs band gap. The Ge absorption lines are plotted in dim colors.

the bottom junction suffers a strong quench for wavelengths shorter than the InGaAs bandgap (vertical red line). The spectral width of the mirror in the HDBR spans between the InGaAs band gap to the small red arrow. This arrows points to a small peak, indicating that the absorption in the Ge has been suppressed as a result of the optical interference in the DBR. The AlGaAs mirror is not able to achieve such transmission suppression. For example, the absorption of the LDBR (1,10) shows a dip around 0.8 μm corresponding to the reflectance window of the DBR. More layers could reduce the transmittance but not the width, as discussed previously. The effect of DBR stacking is illustrated by the LDBR (3, 20), where three different stacks are optimized. The absorption in the Ge junction shows a sequence of narrow dips between 0.7 μm and the InGaAs band gap. As a result, the absorption in the middle junction increases where the dips are located.

5.2 Efficiency of LTS and interstitial selective mirror

5.2.1 Efficiency of the LTS structure

After studying the enhancement introduced when a bilayer ARC is combined with an interstitial mirror, we proceed to substitute the bilayer by an LTS comprising a moth eye photonic structure. The parameters defining the structure are the lattice constant a_{m}, cone height h_{m}, cone radius r_{m}, base h_{b} and spacer h_{s}. The material system is TiO_2 for the cone and base and Si_3N_4 for the spacer. The interstitial mirror is defined as in the previous section. The optimization results are shown in Fig. 13. The three panels contain the same results but are displayed differently. In Fig. 13(a), we present the total efficiency of the tandem solar cell for only three types of mirrors. Those are the most representative from the study of Section 5.1: SPM, HDBR and LDBR (1, 10) (in the following we refer to this latter structure as LDBR). The SPM is the structure which provides the best performance. The HDBR is the closest physical realization of the SPM. Finally, LDBR is the closest model to the actual 3G30 SC. We have also included the results of the bilayer ARC obtained

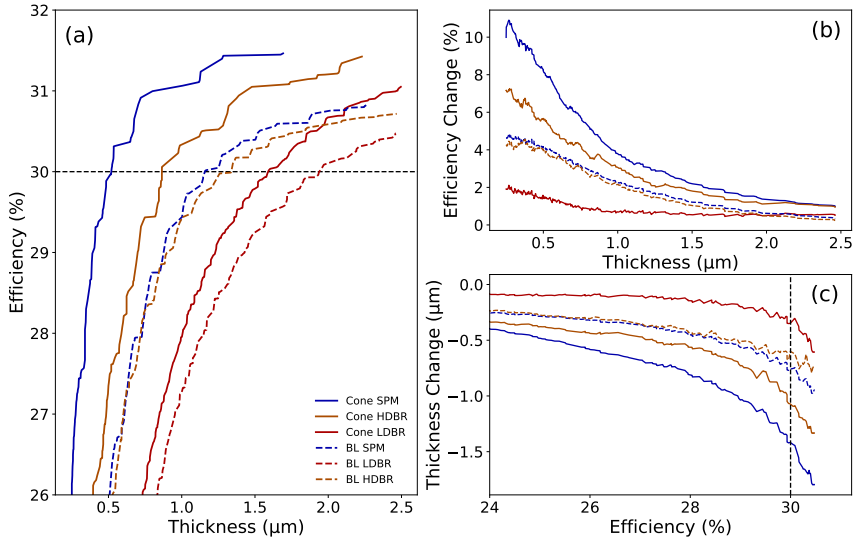

Figure 13: (a) Total efficiency of the tandem solar cells as function of the InGaAs thickness. The solid curves correspond to the LTS structures and the dashed one to the ARC structures. Colors are the same for equal interstitial mirror. (b) Change in efficiency of each LTS structure with respect to the ARC with LDBR (1, 10). (c) Change in thickness of the InGaAs layer as a function of the efficiency for the same cases as in (b).

previously, as a reference. In all cases the LTS shows a great improvement in efficiency. This is more dramatic for thin InGaAs thicknesses. For thicker h_{InGaAs}, the middle junction absorbs enough light and therefore the enhancement is not so remarkable. Still, the fact of showing a modest improvement is a clear indication that light-trapping is added to the bare anti-reflective effect.

The dashed line is the target efficiency of the 3G30 SC, i.e. approximately 30 %. The fact that LDBR takes that value at 1.93 µm is a good indication of the validity of our physical model, as the middle junction of the 3G30 is about 1.8 µm[1]. It is also noteworthy that the efficiency is not very sensitive to the thickness around this value. In the following, we will discuss the change in efficiency at a given h_{InGaAs} and, conversely, the change in h_{InGaAs} at a given efficiency, with respect to the results of the ARC LDBR case.

Fig. 13(a) shows the aforementioned change in efficiency. These results serve to establish what is the benefit of improving the reflectance spectral window of the mirror together with the introduction of an LTS. The LTS provides an increase of 1 % for thicknesses greater than 1 µm, only for thinner cases the increase can reach a 2 %. This enhancement is smaller than the bilayer with a SPM. However, when the mirror is replaced by the TiO_2 DBR, it is possible to get a better conversion for all thicknesses, again being more pronounced in the thin region. The HDBR is a system which sets the maximum efficiency attainable with actual physical structures. Such efficiencies can be reached by LDBR stacks of large M and N as shown in Fig. 11. The highest efficiency is hence obtained by combining the LTS with the SPM. Increases greater than 4 % can be found for thicknesses smaller than 1.0 µm.

Concerning the original question on the radiation hardness of the SC, we show in Fig. 13(c) the reduction in h_{InGaAs} for equal values of efficiencies. For a target efficiency of 30 %, we can see the thickness matching that value for each proposal. The general trend is that photonic solutions

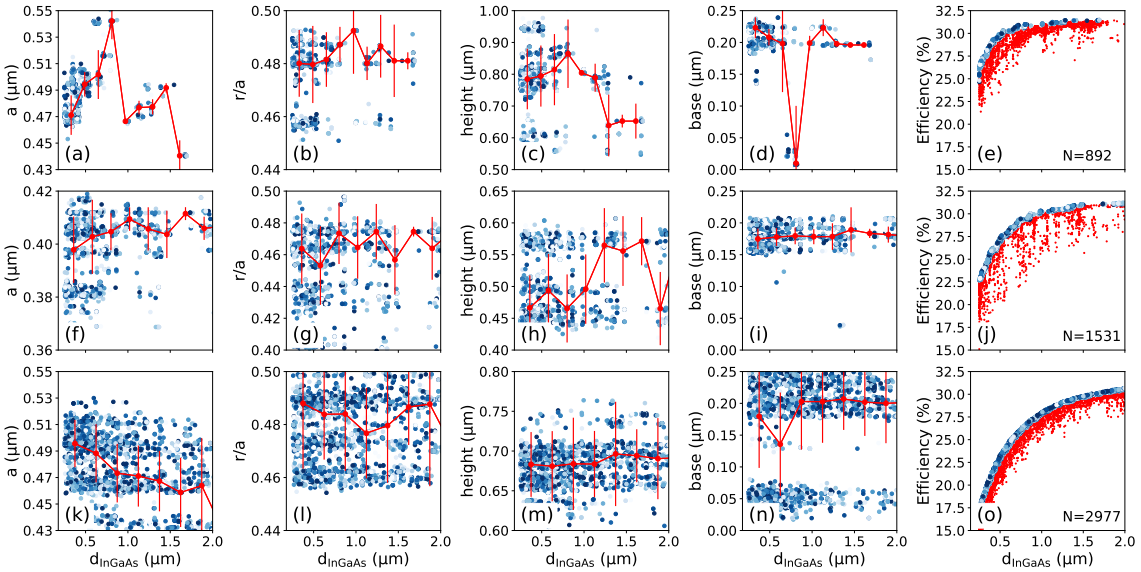

Figure 14: Optimized LTS parameters. (a-e) SPM case, (f-j) HDBR case and (k-o) LDBR case. The colour intensity of the points correspond to its non-dominant rank. The number of solutions of each case is indicated in (e), (j) and (o).

provide a highest reduction in thickness precisely in the region of highest efficiencies. Introducing the LTS results in a 350 nm thinner layer. The reduction is 750 nm, 1070 nm, and 1400 nm for the bilayer with SPM, LTS with HDBR and LTS with SPM, respectively. The potential of improvement is notorious and justifies a further exploration of physical structures, which can bring these new concepts into actual solar cells.

5.2.2 Structural parameters of LTS

Once the different structures are optimized, it is possible to analyze the values taken by the structural parameters defining the LTS. We show these results for the three main problems described so far: SPM, HDBR and LDBR in Figure 14. Each dot corresponds to an optimized problem. The color indicates its non-domination rank, being the darkest the lowest rank. Solutions belonging to the rank zero constitute the Pareto-optimal font introduced in Section 3.5, i.e. the optimal compromise between efficiency and InGaAs thickness. Higher rank values depart from these optimal front. We have only included in Fig. 14 solutions with a rank ≤ 10. The rightmost panels [Figs. 14(e), 14(j) and 14(o)] show all the solutions found by the algorithm in red with the chosen ones in foreground. We have also included in each plot the median and standard deviation (red dots and bars) for 10 bins.

The general trend is that there is not a clear optimal structure able to maximize the efficiency for any value of h_{InGaAs}. The median of each parameter shows the trend identified by the algorithm. For example, the lattice parameter in the SPM case (Fig. 14(a)) shows a clear jump with h_{InGaAs}. For a thin middle junction, the lattice parameter ranges from 470 nm up to 550 nm. This behaviour can be explained by the fact that a guided mode is red-shifted when the InGaAs layer broadens. The algorithm adjusts not only the lattice constant but the other parameters to stay tuned to this resonance. However, for an InGaAs layer thicker than 1.0 µm, a jump in the lattice constant takes place, meaning that the structure can enter in resonance with a different guided mode. Such

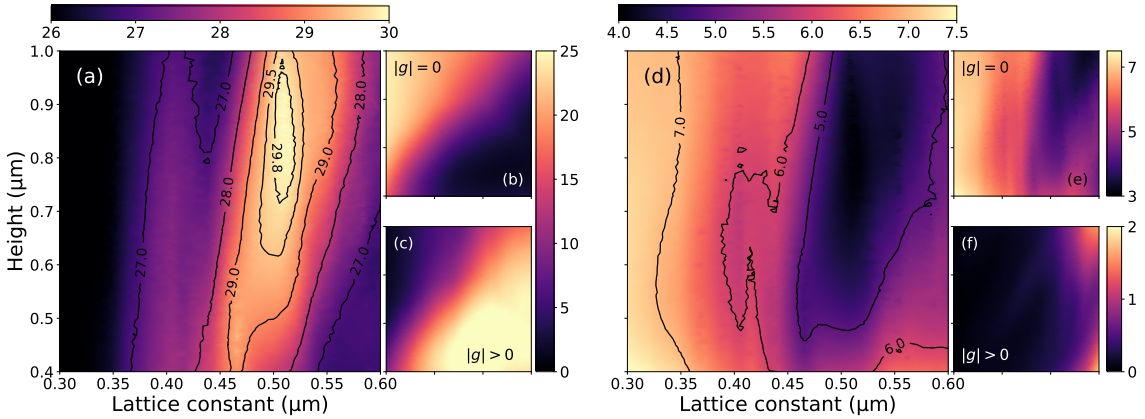

Figure 15: Contour plots for the SPM case showing the dependence of the efficiency (a) and reflectance (d) on the a_m and h_m. Contribution from the zeroth diffraction order (b) and (e) and higher diffraction orders (c) and (f). The reference structure is defined for $h_{InGaAs} = 491$ nm, $a_m = 502$ nm, $r_m/a_m = 0.49$, $h_m = 856$ nm, $h_b = 224$ nm and $h_s = 2$ nm. This solution belongs to the non-dominated front of rank 0.

explanation is also supported by the increase in reflection losses that take place when the more diffraction channels open in the front medium. More details are presented in the discussion of Figure 15. Structures HDBR and LDBR does not exhibit such jumps. In these structures, the excitation of the guided modes is weaker as the modes are less confined in the absorbing layers.

Two very important parameters from the point of view of fabrication are h_m and h_b. The sum of both gives the total amount of TiO_2 needed in achieving the maximum efficiency in the solar cell. In all cases the optimization indicates that values between 600 nm and 1000 nm are needed. This posses a problem for the fabrication of the LTS as high refractive index and hence high crystal quality TiO_2 can only be produced in very thin layers, typically up to 100 nm [48]. Indeed, the reported refractive index for micron-size cones is 2.3 at 400 nm, significantly smaller than the value used in this work [23] (2.88 at 400 nm).

It is interesting to get a broad picture of the dependence of the two main parameters defining the dependence of the LTS on the efficiency, a_m and h_m. Figure 15(a) shows a contour plot of the efficiency of a particular solution of the SPM structure varying these two parameters. The efficiency varies more notably across the lattice parameter axis than across the height axis. A clear maximum can be distinguished at the values found by the optimizer ($h_m = 856$ nm and $a_m = 502$ nm). The elliptical shape of the contour lines makes even more evident the critical dependence on a_m.

The LTS acts as a diffraction grating. This means that part of the incoming light is transferred into diffraction orders that propagate inside of the solar cell at a different angle. Only the zeroth order is not diffracted and is characterized by a reciprocal lattice vector of zero norm ($|g| = 0$). Fig.15(b) shows the contribution to the efficiency of that order. The contribution of the higher diffraction orders ($|g| > 0$) is shown in Fig.15(c). The highest efficiency of each contribution is found in different regions of the plot, being the global maximum of Fig. 15(a) found in the overlap zone. Hence, none of the contributions is dominant, the maximum efficiency is where both balance each other.

Outside of the solar cell, the LTS introduces reflection losses by back diffracting the incoming light. Figure15(d) shows the average reflection as a function of the cone height and lattice constant.

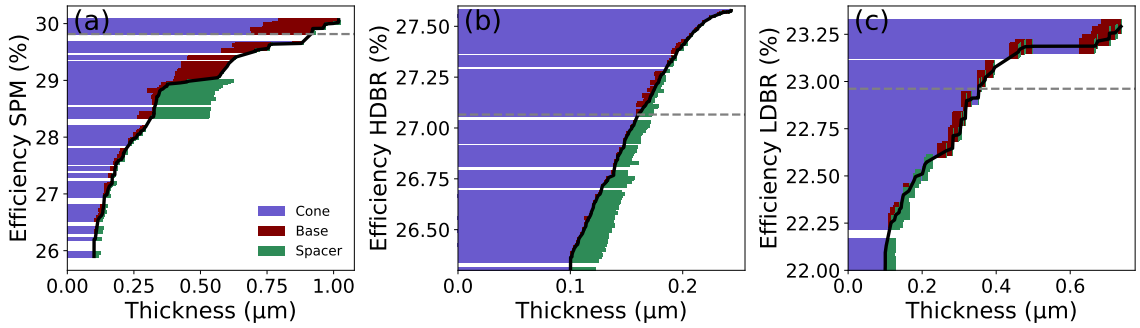

Figure 16: Multiobjetive optimization of the efficiency versus cone height plus base thickness, i.e. TiO_2 amount, for SPM (a), HDBR (b) and LDBR (c) for $h_{\mathrm{InGaAs}} = 0.5\,\mu\mathrm{m}$. Black solid line is the Pareto-optimal front. Each panel contains a horizontal bar plot with the contribution of the cone height (purple bar), base (maroon bar) and spacer thickness (green bar). The dashed line is the efficiency found in Fig. 13. For the sake of clarity, the axes scales are different in each panel.

It shows a complementary behaviour to the efficiency shown in Figure15(a), the efficiency takes its minimum value when the reflection is maximal and vice versa. Here again, a_{m} is more critical than h_{m}. We also show the contribution to reflection of the zeroth (Fig. 15(e)) and higher diffraction orders (Fig. 15(f)). As a_{m} increases, the reflection through the zeroth order decreases. In contrast, for the higher orders, the reflection is very small until a_{m} is greater than its optimal value. The conclusion is that the mechanism limiting the efficiency is the sudden increase of reflection by the back diffracted light. As a_{m} increases, more diffraction channels open in the cover glass of the solar cell [59]. The first diffraction order gets open at $\lambda_1 = n_{\mathrm{cover}} a_{\mathrm{m}}$, i.e. at $\lambda_1 = 703$ nm for $a_{\mathrm{m}} = 502$ nm and $n_{\mathrm{cover}} = 1.4$. The high diffraction orders only carry energy for $\lambda < \lambda_1$, therefore, for larger a_{m}, part of the light that could eventually be absorbed in the middle junction is reflected. A trade-off is established between the amount of light that is reflected (Fig. 15(f)) or diffracted inside of the solar cell (Fig. 15(c)).

5.3 Fabrication issues

From the point of view of the LTS fabrication, we have seen in the previous section that the optimal solutions require thick bases and tall cones.The deposition of high density, high refractive index TiO_2 with low parasitic absorption and high refractive index requires very slow growth rates using Atomic Layer Deposition (ALD), limiting in practice the economically feasible layer thickness. To study what is the efficiency penalty for reducing total amount of TiO_2 needed in the LTS, we have performed a multiobjective optimization for the total efficiency and the total TiO_2 thickness, i.e. h_{m} plus h_{b}. The Pareto-optimal front is shown in Figure 16 for the SPM, HDBR and LDBR structures in a cell of $h_{\mathrm{InGaAs}} = 500$ nm. The lower bound of total thickness is set to 100 nm. The optimal value found in Figure 13(a) for the current cell is indicated in each plot by a dashed horizontal line. The difference in efficiency is always smaller than 0.5 % showing that a detailed optimization for a fixed h_{InGaAs} provides a slightly better result validating the approach followed in the previous section. The total penalty in the efficiency is 4 %, 1.25 % and 1.3 % for SPM, HDBR and LDBR, respectively. However, quite different behaviour is found for the three studied structures.

SPM is able to increase the solar cell efficiency up to the upper bound of 1 μm with an remarkable change in the slope of the Pareto-optimal front. A change of 3 % is found up to a total thickness of 0.4 μm while, from that value to the upper bound, the improvement is only of 1 %.

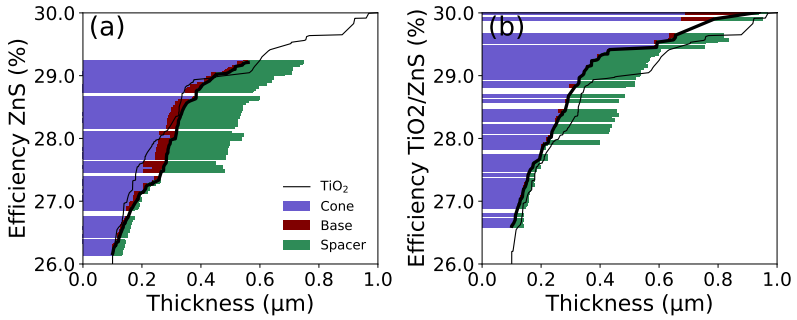

Figure 17: Same optimization as in Fig. 16 for SPM but ZnS replacing TiO_2 (a) and ZnS replacing Si_3N_4 (b) for h_{InGaAs} = 0.5 µm. Black thin line is the Pareto non-dominant front of SPM.

The final layout of the structure can be inferred from the horizontal bar plot. Each bar contains the contribution to the total height of the cone and base together with the spacer. In general, the spacer is very small in the SPM, although there is a region (efficiencies between 28 % and 29 %) where it helps in keeping the high slope of the front. At higher efficiency values, the base takes larger values as only the high refractive index of TiO_2 is able to keep increasing the efficiency.

The HDBR structure shows a very narrow range of efficiencies for improvement. Indeed, the optimizer is not able to find better efficiencies for thicknesses beyond 250 nm. The curve shown in Fig. 16(b) is very similar to that of the SPM in Fig. 16(a) in the same range of thicknesses. For both structures the spacer takes a value of $\approx$ 25 nm and reduces as the efficiency increases. The maximum efficiency of the HDBR is 27.5 % at a total thickness of 250 nm. At this thickness, the SPM is only marginally better at 28 % efficiency.

Finally, the LDBR structure shows an enhancement of the efficiency from 22 % for 100 nm of total thickness to 23.3 % for 737 nm. Again, in this structure the spacer is only meaningful in the region of small cones.

An alternative approach to face the fabrication issues associated to TiO_2 is to use a material of lower refractive index but higher than Si_3N_4. This is for example the case of ZnS, a semiconductor extensively used by the optoelectronic industry. In our context, ZnS also helps in showing the impact of reducing the quality of TiO_2 which would result in a lower refractive index. The results of a multiobjective optimization similar to that presented above for the SPM structure is shown in Fig. 17(a). The general behavior is similar to the TiO_2 case for efficiencies up to 29 %. This is consistent with the role of the spacer discussed in Fig. 16(a). Hence, reaching the highest performance region requires not only of tall cones, but of high refractive index material as well. The comparison with the TiO_2 can be inferred by the thin solid line. The achievable efficiency as a function of the thickness is very similar for both cases. It is then possible to reach 29 % efficiency with a total thickness of 590 nm using either TiO_2 or ZnS.

In all the structures implemented so far we have used a low refractive index spacer made of Si_3N_4. In Fig. 17(b) we show what would be the effect of using ZnS for the spacer and TiO_2 for cone and base. This material combination is able to enhance the efficiency in almost the whole range of thicknesses. The base is almost neglected and only relevant in the top range of efficiencies. A remarkable result is the existence of a solution requiring only a $h_m \approx 420$ nm TiO_2 cone with an efficiency of 29.4 %. Such efficiency is only reached in the TiO_2 case (thin black line) at $h_m + h_b \approx 630$ nm.

6 Conclusions

We have studied two light-trapping structures inspired by biological designs, namely moth's eyes (ME) and diatoms (DA). We describe the solar cell efficiency with two different physical models focused either in the BOL or the EOL efficiency. The BOL model does not take into account the details of the doping distribution in the junction and therefore is only applied in the optimization of the LTS structures. The optimal structures for both designs confirm that it is possible to notably reduce the middle junction thickness while keeping the BOL efficiency of the reference thickness $h_{\mathrm{InGaAs}} \approx 1.8\,\mu\mathrm{m}$.

The DA structures allows to halve that thickness while the ME allows a reduction down to a third. These results, although very promising, have been critically revised. Firstly, the ideal collection of the carriers in the junction is reviewed in the EOL efficiency. There we find that the radiation hardness can be notably enhanced by both LTSs with respect to a bilayer ARC with a slighter better performance of the ME over the DA in the region of high damage level. We have also shown that the radiation damage depends on the particle nature of the radiation and its energy, being almost insensitive to the type of LTS or the layer thickness. We have identified the increase of the collection efficiency as the only mechanism increasing the radiation hardness of the space solar cell.

Secondly, the optimal LTS was calculated with an ideal selective perfect mirror. When such approximation is relaxed by introducing a realistic DBR, the reduction in thickness is very dependent on the reflectance value and width of the DBR. Hence, a DBR based on a single stack of AlGaAs/AlAs only allows for a modest reduction of h_{InGaAs} without sacrificing the efficiency ($\approx 350\,\mathrm{nm}$). The reduction is notably enhanced to $1.0\,\mu\mathrm{m}$ by introducing a DBR of higher index contrast such as TiO_2/SiO_2. This opens the possibility to get a new design of the 3G30 by finding a multi-stack or disordered DBR with a performance similar to that of TIO_2/SiO_2. Even more interesting is the fact that the SPM sets an even larger value of the h_{InGaAs} reduction, opening the door to seek for more challenging proposals to replace the interstitial mirror, like nanoparticle arrangements or diffraction gratings. An additional difficulty that needs to be faced in applying this proposals to industrial space solar cell structures is the thickness and height of the layers involved in the LTS, either inspired by DA or ME. However, we have also seen that the efficiency penalty can be as low as 1 % if the high refractive index material, like TiO_2 is replaced by a material of lower refractive index like ZnS.

In summary, we present a technological route to enhance the radiation hardness of space solar cells. We described the challenges and difficulties to introduce these enhancements, and provide ways to overcome them. We are confident that in the short term, solar cells like the 3G30 could experience an important reduction in thickness, thus reducing their production cost and increasing their EOL efficiency, contributing to increasing the reliability of power systems of future space missions.

Appendix A 1D diffusion model

The modelling approach of the present section is based on the analytical model of p-n homojunctions and the underlying assumptions found in [60]. Here, we introduce two main differences. First, we assume an arbitrary absorption profile $a(\lambda, x)$ inside the junction in contrast to the commonly exponential profile based on the Beer–Lambert law. This is crucial in order to capture the effect of the LTS on the junction photocurrent. Second, we assume that the recombination velocity at the edges of the junction is low enough that can be neglected.

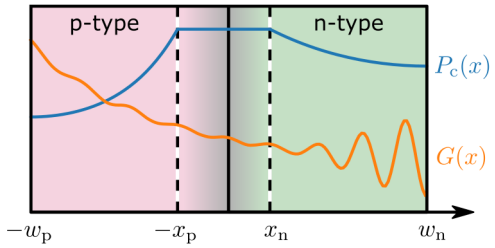

Figure 18: Schematic of the p-n junction used in the 1D diffusion model.

Without loss of generality we assume a p-type emitter of width x_W connected with an n-type base. The junction is divided into three regions as shown in Figure 18; the p-type quasi-neutral area (QNA), the n-type QNA and the depletion region. The origin for the current analysis is placed at the interface between the emitter and the base. The depletion region spans from $-x_p$ to x_n and the p-type and n-type QNAs have width of $\bar{w}_p = w_p - x_p$ and $\bar{w}_n = w_n - x_n$ respectively. The current density of the junction is given sum of the current densities of the QNAs, J_p and J_n, and the depletion region, J_d, as

$$J = J_p + J_n + J_d. \tag{18}$$

First we turn our attention at the n-type QNA, where the excess minority carrier density, δp, follows the diffusion equation

$$\frac{d^2\delta p}{dx^2} - \frac{1}{L_p^2}\delta p + G(x) = 0 \tag{19}$$

where $L_p = \sqrt{\mathcal{D}_p \tau_p}$ is the minority carrier diffusion length and $\mathcal{D}_p$ is the diffusion constant. The generation rate is given, similar to Eq. (1), as

$$G(x) = \frac{\mathcal{D}_p}{hc}\int_0^{\lambda_g} a(\lambda, x)\Phi(\lambda)\lambda d\lambda. \tag{20}$$

Two boundary conditions accompany Eq. (19):

$$\frac{d\delta p}{dx} = 0 \qquad x = w_n \tag{21}$$

$$\delta p = p_0(e^{\frac{E_{Fp}}{kT}} - 1) \qquad x = x_n \tag{22}$$

where p_0 is the equilibrium hole density and E_{Fp} is the quasi-Fermi level. For the sake of convenience, we shift the origin of the x-axis at the interface between the n-type QNA and the depletion zone. We denote the coordinates at the shifted system by $\bar{x} = x - x_n$. We obtain the solution to Eq. (19) using the Green's function approach. The Green's function satisfies

$$\frac{d^2\mathcal{G}(\bar{x}, s)}{d\bar{x}^2} - \frac{1}{L_p^2}\mathcal{G}(\bar{x}, s) = \delta(\bar{x} - s) \tag{23}$$

with $\delta(\bar{x} - s)$ Dirac's δ function. The general solution to Eq. (23) is of the form

$$\mathcal{G}(\bar{x}, s) = \begin{cases} c_1(s)\cosh\left(\frac{\bar{x}}{L_p}\right) + c_2(s)\sinh\left(\frac{\bar{x}}{L_p}\right) & \bar{x} < s \\ c_3(s)\cosh\left(\frac{\bar{x}}{L_p}\right) + c_4(s)\sinh\left(\frac{\bar{x}}{L_p}\right) & \bar{x} \geq s \end{cases} \tag{24}$$

where the coefficients c_1 to c_4 depend solely on s. At the point $\bar{x} = s$, $\mathcal{G}(\bar{x}, s)$ is continuous and satisfies Eq. (23), resulting in

$$c_1 - c_3 = L_\mathrm{p} \sinh\left(\frac{s}{L_\mathrm{p}}\right) \tag{25}$$

$$c_4 - c_2 = L_\mathrm{p} \cosh\left(\frac{s}{L_\mathrm{p}}\right). \tag{26}$$

Given $\mathcal{G}(\bar{x}, s)$, the excess minority carrier density becomes

$$\begin{aligned} \delta p(\bar{x}) &= -\int_0^{\bar{w}_\mathrm{n}} \mathcal{G}(\bar{x}, s) G(s) ds \\ &= \bar{c}_1 \cosh\left(\frac{\bar{x}}{L_p}\right) + \bar{c}_2 \sinh\left(\frac{\bar{x}}{L_\mathrm{p}}\right) - \int_0^{\bar{x}} L_\mathrm{p} \sinh\left(\frac{\bar{x} - s}{L_\mathrm{p}}\right) G(s) ds \end{aligned} \tag{27}$$

where $\bar{c}_1 = -\int_0^{\bar{w}_\mathrm{n}} c_1 G ds$ and $\bar{c}_2 = -\int_0^{\bar{w}_\mathrm{n}} c_2 G ds$. We note that the last integral in Eq. (27) is the convolution of the kernel $L_\mathrm{p} \sinh(\bar{x} L_\mathrm{p}^{-1})$ with the generation rate. The remaining constants can be determined by applying the boundary conditions:

$$\bar{c}_1 = p_0(e^{\frac{V}{kT}} - 1) \tag{28}$$

$$\bar{c}_2 = \int_0^{\bar{w}_\mathrm{n}} \frac{L_\mathrm{p}}{\cosh\left(\frac{\bar{w}_\mathrm{n}}{L_\mathrm{p}}\right)} \cosh\left(\frac{\bar{w}_\mathrm{n} - s}{L_\mathrm{p}}\right) G(s) ds - \bar{c}_1 \tanh\left(\frac{\bar{w}_\mathrm{n}}{L_\mathrm{p}}\right) \tag{29}$$

where we have substituted $E_{Fp} = V$ under the assumption that the quasi-Fermi level is constant throughout the depletion region [60]. The current density is calculated from the derivative of δp as

$$J_\mathrm{p} = -e\mathcal{D}_\mathrm{p} \frac{d\delta p(0)}{dx} = -\frac{e\mathcal{D}_\mathrm{p}}{L_\mathrm{p}} \bar{c}_2, \tag{30}$$

where e is the elementary charge constant. The last member of Eq. (30) results of differenciating Eq. (27). Two contributions can be identified in $\bar{c}_2$. The first comes from the photocurrent, which is computed as the integral of generation rate in the QNA multiplied by the collection probability

$$P_\mathrm{c}(\bar{x}) = \cosh\left(\frac{\bar{w}_\mathrm{n} - \bar{x}}{L_\mathrm{p}}\right) \left[\cosh\left(\frac{\bar{w}_\mathrm{n}}{L_\mathrm{p}}\right)\right]^{-1}. \tag{31}$$

The second term depends on the applied voltage and contributes to the diode saturation current.

An identical analysis can be performed in the p-region, with J_n given by a relation analogous to Eq. (30). For the depletion area, we assume complete photocarrier collection and a contribution to the saturation current independent of τ_p and τ_n, given from Eq. (3). Adding the current density of the QNAs and the depletion area, the photocurrent is computed as in Eq. (7), with

$$P_\mathrm{c}(x) = \begin{cases} \cosh\left(\frac{w_\mathrm{p} + x}{L_\mathrm{n}}\right) \left[\cosh\left(\frac{\bar{w}_\mathrm{p}}{L_\mathrm{n}}\right)\right]^{-1} & x \leq -x_\mathrm{p} \\ 1 & -x_\mathrm{p} < x < x_\mathrm{n} \\ \cosh\left(\frac{w_\mathrm{n} - x}{L_\mathrm{p}}\right) \left[\cosh\left(\frac{\bar{w}_\mathrm{n}}{L_\mathrm{p}}\right)\right]^{-1} & x \geq x_\mathrm{n} \end{cases} \tag{32}$$

and the increase in the saturation current by

$$J_{\mathrm{d}0} = \frac{q\mathcal{D}_\mathrm{p} p_0}{L_\mathrm{p}} \tanh\left(\frac{\bar{w}_\mathrm{n}}{L_\mathrm{p}}\right) + \frac{q\mathcal{D}_\mathrm{n} n_0}{L_\mathrm{n}} \tanh\left(\frac{\bar{w}_\mathrm{p}}{L_\mathrm{n}}\right) \tag{33}$$

Table 3: Comparison of D_d [arb.u.] for single (SSC) and combined single/multiple scattering (MSC) models.

source		SSC	MSC
electron	1 MeV	0.021 ± 0.002	0.020 ± 0.002
electron	5 MeV	0.054 ± 0.009	0.052 ± 0.008
proton	3 MeV	14.875 ± 0.671	14.918 ± 0.683
proton	10 MeV	6.084 ± 1.200	6.154 ± 1.058

where n_0 is the equilibrium minority carrier concentration. We point out that for $L_p \gg w_p$ and $L_n \gg w_n$, we retrieve the original model, with collection probability equal to 1 throughout the junction and no contribution to the saturation current from the QNAs.

The values for $\mathcal{D}_p$ and $\mathcal{D}_n$ for GaAs were computed using the relations from [61] under the assumption that the minority carrier mobility is equal the majority carrier mobility at any given region. The variables describing the depletion region x_p, x_n, p_0 and x_0 are computed using the abrupt junction approximation under the assumption that the majority carrier concentration is equal to the dopant concentration.

Appendix B Geant4 validation and simulation details

All simulations were performed using the dedicated physics list for space radiation environment (QBBC) [62], with the multiple scattering model being substituted by a single scattering one at the middle junction. It is possible to track the PKAs in the semiconductor material, only if the dedicated single Coulomb scattering physics [35, 63] are selected in the Geant4 physics list. The single scattering model though is computationally more expensive than the commonly used multiple scattering model [64] and its use is restricted when the highest possible accuracy is needed.

We are interested in the PKAs occurring in the middle junctions, which constitutes less than 1.5 % of the total thickness of the solar cell stack. To keep the simulations time within reasonable limits, we combine the multiple and single scattering models in our code. The layers of the solar cell are grouped in two regions: a) layers where the D_d needs to be calculated and b) the remaining layers. For the first region, the single scattering model was selected and the secondary production range cut was set to 40 nm, whereas for the second region the multiple scattering is used and the secondary production range cut was set to 400 nm. We validated the code by comparing the simulations results to the ones with uniform single scattering model and 40 nm secondary production range cut over the whole cell geometry. Table 3 contrasts the D_d values from the two implementations for monoenergetic 1 MeV and 5 MeV electron, and 3 MeV and 10 MeV proton sources with incident normal to the solar cell for 10^6 primary events. The difference between the computed values lie inside the CI bounds. The relative speedup for the single/multiple scattering combined physics list was measured between 41 and 77 times.

Realistic space radiation environment can be constructed for given Earth trajectories. The spectra contains three contributions: trapped electron and protons, and solar protons. In our simulations we considered three orbits: a low-earth orbit at 800 km with 98.0° inclination, a highly elliptical orbit at 700 km × 12 050 km with 63.4° inclination and a geostationary orbit. The trapped particle spectra was determined using the AP-8 and AE-8 models and the solar proton spectrum was calculated from ESP total fluence model, using the software SPENVIS [65]. The integral particle fluence over the time span of one year is shown in Fig. 19.

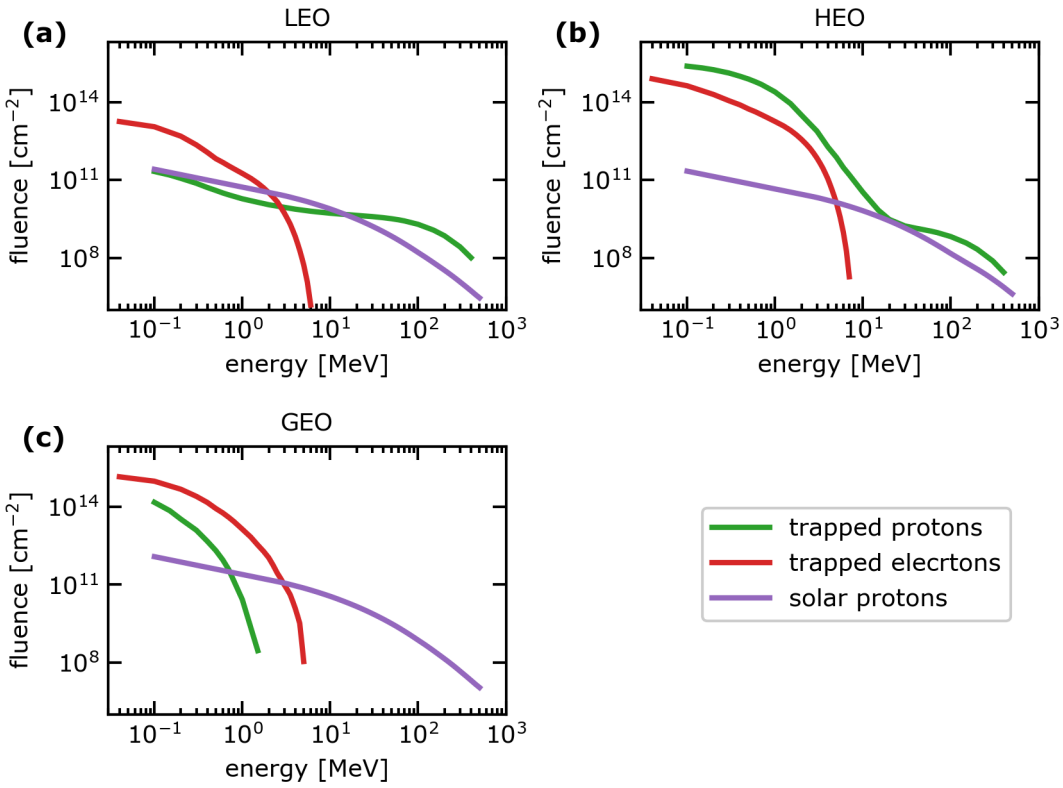

Figure 19: Integral particle fluence over the course of one year for three different orbits. (a) Low earth circular orbit (LEO) at 800 km with 98.0° inclination. (b) Highly elliptical orbit (HEO) at 700 km × 12 050 km with 63.4° inclination. (c) Geostationary orbit (GEO).

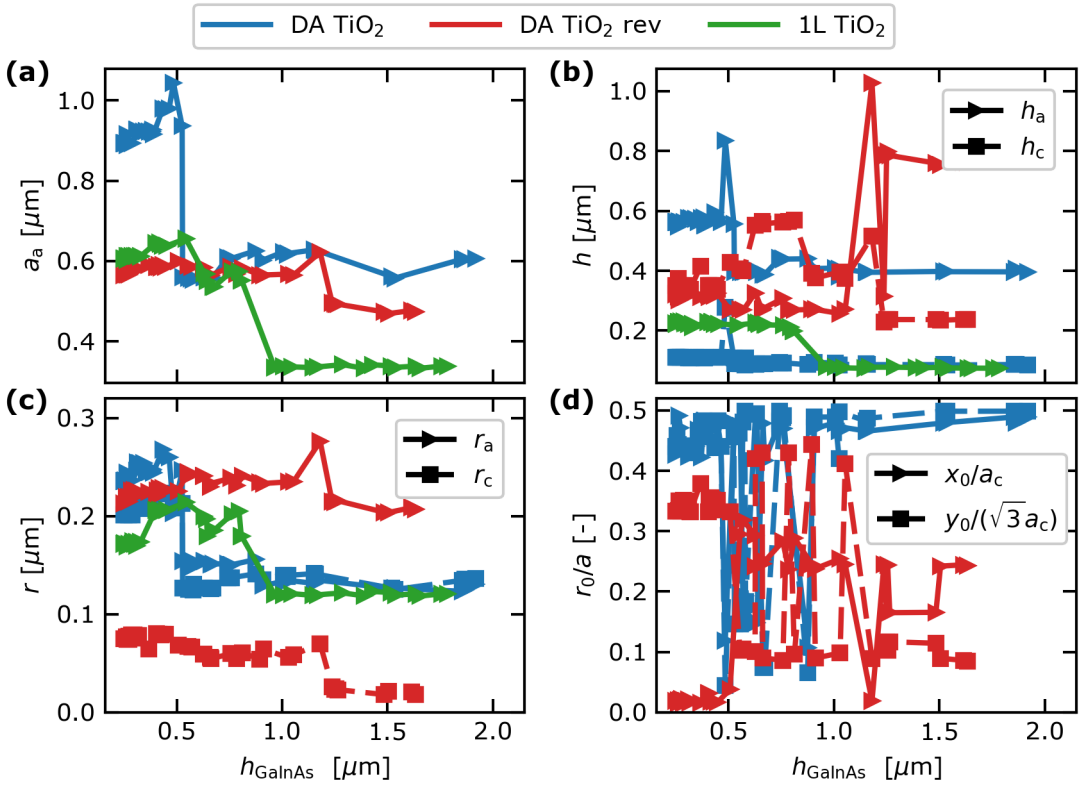

Figure 20: Geometrical parameters for the optimized diatom structures. Parameters for three configurations are shown: normal layer ordering (DA), reversed ordering (DA rev) and single layers with hexagonal pores (1L).

Appendix C Geometrical parameters for optimized LTS

The optimal geometrical parameters of the three structures studied in Figure 7 are gathered in Fig. 20(a)-(d). For the single layer, the optimal a_a assumes roughly two values: around 0.60 µm for $h_{InGaAs} < 0.80$ µm and 0.35 µm for $h_{InGaAs} > 0.80$ µm. This implies that the scattering of light is playing an important role in the former case. Wavelengths smaller than a_a/n_{cover} can be back-diffracted hence introducing reflection losses. In contrast, diffraction inside of the cell is beneficial for light-trapping. A trade-off is established between both processes. Light-trapping is critical for thin absorbers to expand the optical path length and, therefore, a_a is larger than in the case of thick ones. A similar split into two distinct regions is observed for the single layer h_a and r_a parameters. This means that the average refractive index is higher as holes reduce, i.e. that the single layer acts more as a single layer anti-reflective coating than as a light-trapping element for thick InGaAs. This is also supported by the reduction of the h_a approaching towards the typical thickness of an interferential filter.

For the diatom configuration, a_a follows a similar pattern at almost double the value of the single layer, with the transition taking place at $h_{InGaAs} = 0.50$ µm. That means that the cribum lattice constant takes a value very close to that of the single layer. Likewise, the thickness and the pore radius shows the same trend as a_a. As the thickness of the middle junction increases, r_a and r_c converge to the value of 0.12 µm, which coincides with the pore radius for the single layer. The

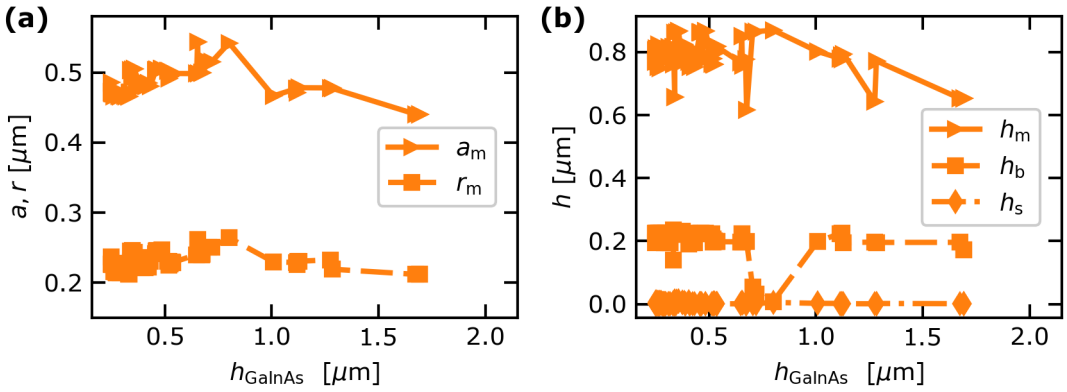

Figure 21: Geometrical parameters for the optimized moth-eye structures.

relative displacement between the two layers has a rather constant value towards the diagonal of the unit cell, with x_0/a_c and $y_0/(\sqrt{3}a_c)$ both adopting values close to 0.5. For the reversed diatom configuration, two regions are present with the transition happening at $h_{\mathrm{InGaAs}} = 1.20\,\mu\mathrm{m}$. The relative displacement in this case seems to play a secondary role in the η enhancement. The geometry of cribrum layer for diatom configuration and the single layer are similar for thick junctions, implying that the areola layer plays a supporting role on the first.

The parameters for the optimized moth-eye (ME) LTS are shown in Figure 21. The lattice constant a_m shows a softer evolution than a_a with h_{InGaAs}. The cones helps in balancing the trade-off between reflection losses and diffracted light if compared with the hole arrangement constituting the diatom structure. Indeed, the ME can be seen as a averaged graded index layer, which helps in reducing the impedance mismatch between the solar cell layers and the cover glass. The radius is always larger than 0.2 µm which means that the cone base tends to completely fill the unit cell area, i.e. $r_m/a_m \approx 0.5$. The cone height h_m takes very large values, close to 800 nm in the region of interest, i.e. for thin middle junctions. The base and spacer thicknesses h_b and h_s are almost constant along the whole optimization range, being the latter almost negligible. If h_c is added to h_m we get the total amount of TiO_2 needed to fabricate the structure. A layer of 1 µm is indeed needed. This is an experimental challenge, as high index and high quality TiO_2 is difficult to obtain beyond 100 nm. More research and alternative proposals will addressed in the future to cope with this issue.

Appendix D Optimal DBR thicknesses

The anti-reflective coating is defined by a MgF_2/ZnS bilayer of thicknesses 82/56 nm for all the DBR cases. Each stack in the DBR is characterized by their filling factor and averaged thickness in Table 4. The optimal values show that for $M > 1$ the optimization algorithm chooses between increasing the number of layer of a given DBR or shifting the reflectance window. E.g. in LDBR (3, 10) the three stacks show a similar ff and $\hat{d}$, meaning, that the reflection window is almost spectrally fixed but with a total larger number of layers.

Table 4: Layer thicknesses in DBR expressed as the filling factor of the high-index layer with respect to the full thickness ($ff = d_{\mathrm{H}}/(d_{\mathrm{H}} + d_{\mathrm{L}})$) and the average thickness $\hat{d} = (d_{\mathrm{H}} + d_{\mathrm{L}})/2$.

Structure	Stack i:[ff, $\hat{d}$ (nm)]		
HDBR	1:[0.330,100.9]		
LDBR (1, 10)	1:[0.345,62.8]		
LDBR (2, 10)	1:[0.245,58.6]	2:[0.479,65.2]	
LDBR (3, 10)	1:[0.508,59.4]	2:[0.569,54.2]	3:[0.498,65.9]
LDBR (4, 10)	1:[0.478,52.7]	2:[0.421,57.9]	3:[0.309,68.9]
	4:[0.486,65.1]		
LDBR (6, 10)	1:[0.540,52.0]	2:[0.512,58.4]	3:[0.445,66.2]
	4:[0.426,66.3]	5:[0.390,62.7]	6:[0.298,56.9]
LDBR (2, 20)	1:[0.666,56.5]	2:[0.401,64.8]	
LDBR (3, 20)	1:[0.357,56.1]	2:[0.723,58.9]	3:[0.489,66.4]

References

[1] W. Guter, F. Dunzer, L. Ebel, K. Hillerich, W. Köstler, T. Kubera, M. Meusel, B. Postels, and C. Wächter. Space solar cells – 3G30 and next generation radiation hard products. *E3S Web of Conferences*, 16:03005, 2017.

[2] R.J. Walters, J.H. Warner, G.P. Summers, S.R. Messenger, and J.R. Lorentzen. Radiation response mechanisms in multijunction III-V space solar cells. In *Conference Record of the Thirty-first IEEE Photovoltaic Specialists Conference, 2005.*, pages 542–547, January 2005. ISSN: 0160-8371.

[3] S. I. Maximenko, M. P. Lumb, J. Moore, L. C. Hirst, M. K. Yakes, and P. P. Jenkins. Thin GaAs Solar Cells For High Irradiation Levels. In *2019 IEEE 46th Photovoltaic Specialists Conference (PVSC)*, pages 2814–2817, June 2019. ISSN: 0160-8371.

[4] R. Cariou, H. Chen, A. Cattoni, K. Medjoubi, J. Lefèvre, B. Boizot, O. Höhn, D. Lackner, F. Dimroth, and S. Collin. Radiation hardness of ultra-thin GaAs solar cells with rear-side silver mirror. In *46th Photovoltaic Specialists Conference (PVSC)*, pages 2811–2813, June 2019.

[5] S. J. Polly, G. T. Nelson, J. R. D'Rozario, R. Tatavarti, and S. M. Hubbard. Radiation Effects in Thinned GaAs Photovoltaics Incorporating DBRs for Improved Radiation Tolerance of Multijunctions. In *2019 IEEE 46th Photovoltaic Specialists Conference (PVSC)*, pages 2818–2821, 2019. ISSN: 0160-8371.

[6] Han Zhou, Jun Xu, Xianghui Liu, Haiwen Zhang, Dantong Wang, Zhihan Chen, Di Zhang, and Tongxiang Fan. Bio-inspired photonic materials: Prototypes and structural effect designs for applications in solar energy manipulation. *Advanced Functional Materials*, 28(24):1705309, 2018.

[7] E. De Tommasi. Light Manipulation by single cells: The case of diatoms. *Journal of Spectroscopy*, page 2490128, 2010.

[8] C. E. Hamm, R. Merkel, O. Springer, P. Jurkojc, C. Maier, K. Prechtel, and V. Smetacek. Architecture and material properties of diatom shells provide effective mechanical protection. *Nature*, 421:841, 2003.

[9] Stuart A. Boden and Darren M. Bagnall. Optimization of moth-eye antireflection schemes for silicon solar cells. *Progress in Photovoltaics: Research and Applications*, 18(3):195–203, 2010.

[10] J. Tommila, V. Polojärvi, A. Aho, A. Tukiainen, J. Viheriälä, J. Salmi, A. Schramm, J. M. Kontio, A. Turtiainen, T. Niemi, and M. Guina. Nanostructured broadband antireflection coatings on AlInP fabricated by nanoimprint lithography. *Solar Energy Materials and Solar Cells*, 94(10):1845–1848, 2010.

[11] Juha Tommila, Arto Aho, Antti Tukiainen, Ville Polojärvi, Joel Salmi, Tapio Niemi, and Mircea Guina. Moth-eye antireflection coating fabricated by nanoimprint lithography on 1 eV dilute nitride solar cell. *Progress in Photovoltaics: Research and Applications*, 21(5):1158–1162, 2013.

[12] Jung Woo Leem, Jae Su Yu, Dong-Hwan Jun, Jonggon Heo, and Won-Kyu Park. Efficiency improvement of III-V GaAs solar cells using biomimetic TiO_2 subwavelength structures with wide-angle and broadband antireflection properties. *Solar Energy Materials and Solar Cells*, 127:43–49, Aug 2014.

[13] Mu-Min Hung, Hau-Vei Han, Chung-Yu Hong, Kuo-Hsuan Hong, Tung-Ting Yang, Peichen Yu, Yu-Rue Wu, Hong-Yih Yeh, and Hong-Cheng Huang. Compound biomimetic structures for efficiency enhancement of $Ga_{0.5}In_{0.5}P$/GaAs/Ge triple-junction solar cells. *Optics Express*, 22(102):A295–A300, 2014.

[14] J. Buencuerpo, J. M. Llorens, M. L. Dotor, and J. M. Ripalda. Broadband antireflective nano-cones for tandem solar cells. *Optics Express*, 23(7):A322–A336, April 2015.

[15] J. Buencuerpo, L. Torné, R. Álvaro, J. M. Llorens, M. L. Dotor, and J. M. Ripalda. Nano-cones for broadband light coupling to high index substrates. *Scientific Reports*, 6(1):38682, July 2016.

[16] D. G. Stavenga, S. Foletti, G. Palasantzas, and K. Arikawa. Light on the moth-eye corneal nipple array of butterflies. *Proceedings of the Royal Society B: Biological Sciences*, 273(1587):661–667, March 2006.

[17] Deying Xia, Zahyun Ku, SC Lee, and SRJ Brueck. Nanostructures and functional materials fabricated by interferometric lithography. *Advanced materials*, 23(2):147–179, 2011.

[18] Benedikt Bläsi, N Tucher, O Höhn, V Kübler, T Kroyer, Ch Wellens, and H Hauser. Large area patterning using interference and nanoimprint lithography. In *Micro-Optics 2016*, volume 9888, page 98880H, 2016.

[19] Xiangfan Chen, Chen Wang, Evan Baker, and Cheng Sun. Numerical and experimental investigation of light trapping effect of nanostructured diatom frustules. *Scientific Reports*, 5:11977, July 2015.

[20] Victor Liu and Shanhui Fan. S4 : A free electromagnetic solver for layered periodic structures. *Computer Physics Communications*, 183(10):2233–2244, October 2012.

[21] Luis V. Rodríguez-de Marcos, Juan I. Larruquert, José A. Méndez, and José A. Aznárez. Self-consistent optical constants of MgF_2, LaF_3, and CeF_3 films. *Optical Materials Express*, 7(3):989–1006, March 2017.

[22] Marvin Querry. Optical constants of minerals and other materials from the millimeter to the ultraviolet. Technical Report ADA192210, Chemical Research, Development & Engineering Center, US Army Armament, November 1987.

[23] S. Tanemura, L. Miao, P. Jin, K. Kaneko, A. Terai, and N. Nabatova-Gabain. Optical properties of polycrystalline and epitaxial anatase and rutile TiO2 thin films by rf magnetron sputtering. *Applied Surface Science*, 212-213:654–660, May 2003.

[24] Edward D. Palik, editor. *Handbook of optical constants of solids*, volume 3. Academic press, 1998.

[25] Hirokazu Kato, Sadao Adachi, Hiroshi Nakanishi, and Kouji Ohtsuka. Optical properties of $(Al_xGa_{1-x})_{0.5}In_{0.5}P$ quaternary alloys. *Japanese Journal of Applied Physics*, 33(1A):186–192, January 1994.

[26] Mathias Schubert, V. Gottschalch, Craig M. Herzinger, Huade Yao, Paul G. Snyder, and John A. Woollam. Optical constants of $Ga_xIn_{1-x}P$ lattice matched to GaAs. *Journal of Applied Physics*, 77(7):3416–3419, April 1995.

[27] R. Ferrini, G. Guizzetti, M. Patrini, A. Parisini, L. Tarricone, and B. Valenti. Optical functions of InGaP/GaAs epitaxial layers from 0.01 to 5.5 eV. *The European Physical Journal B - Condensed Matter and Complex Systems*, 27(4):449–458, June 2002.

[28] Timothy Nathan Nunley, Nalin S. Fernando, Nuwanjula Samarasingha, Jaime M. Moya, Cayla M. Nelson, Amber A. Medina, and Stefan Zollner. Optical constants of germanium and thermally grown germanium dioxide from 0.5 to 6.6eV via a multisample ellipsometry investigation. *Journal of Vacuum Science & Technology B*, 34(6):061205, 2016.

[29] John F. Geisz, Myles A. Steiner, Iván García, Ryan M. France, William E. McMahon, Carl R. Osterwald, and Daniel J. Friedman. Generalized optoelectronic model of series-connected multijunction solar cells. *IEEE Journal of Photovoltaics*, 5(6):1827–1839, November 2015.

[30] Jose M. Ripalda, Jerónimo Buencuerpo, and I. García. Solar cell designs by maximizing energy production based on machine learning clustering of spectral variations. *Nature communications*, 9(1):1–8, 2018.

[31] C. Baur, M. Gervasi, P. Nieminen, S. Pensotti, P.g. Rancoita, and M. Tacconi. NIEL dose dependence for solar cells irradiated with electrons and protons. In *Astroparticle, Particle, Space Physics, Radiation Interaction, Detectors and Medical Physics Applications*, volume 8, pages 692–707. World Scientific, April 2014.

[32] M. A. Cappelletti, A. P. Cédola, and E. L. Peltzer y Blancá. Computational analysis of the maximum power point for GaAs sub-cells in InGaP/GaAs/Ge triple-junction space solar cells. *Semiconductor Science and Technology*, 29(11):115025, October 2014.

[33] Roberta Campesato, Carsten Baur, Mariacristina Casale, Massimo Gervasi, Enos Gombia, Erminio Greco, Aldo Kingma, Pier Giorgio Rancoita, Davide Rozza, and Mauro Tacconi. Effects of irradiation on triple and single junction InGaP/GaAs/Ge solar cells. In *35th European Photovoltaic Solar Energy Conference and Exhibition*, pages 959–964. WIP, November 2018.

[34] Claude Leroy and Pier-Giorgio Rancoita. *Principles of radiation interaction in matter and detection*. World Scientific Publishing, second edition, 2009.

[35] M. J. Boschini, C. Consolandi, M. Gervasi, S. Giani, D. Grandi, V. Ivanchenko, S. Pensotti, P. G. Rancoita, and M. Tacconi. Nuclear and non-ionizing energy-loss for Coulomb scattered particles from low energy up to relativistic regime in space radiation environment. In *Cosmic Rays for Particle and Astroparticle Physics*, pages 9–23. World Scientific, 2011.

[36] D. Codegoni, A. Colder, N. Croitoru, P. D'Angelo, M. DeMarchi, G. Fallica, A. Favalli, S. Leonardi, M. Levalois, P. Marie, R. Modica, P. G. Rancoita, and A. Seidman. Investigation of irradiated monolithic transistors for space applications. *Nuclear Instruments and Methods in Physics Research Section B: Beam Interactions with Materials and Atoms*, 217(1):65–76, March 2004.

[37] S. R. Messenger, E. A. Burke, M. A. Xapsos, G. P. Summers, R. J. Walters, Jun Insoo, and T. Jordan. NIEL for heavy ions: an analytical approach. *IEEE Transactions on Nuclear Science*, 50(6):1919–1923, December 2003.

[38] Insoo Jun, Wousik Kim, and Robin Evans. Electron nonionizing energy loss for device applications. *IEEE Transactions on Nuclear Science*, 56(6):3229–3235, December 2009.

[39] Insoo Jun, M. A. Xapsos, S. R. Messenger, E. A. Burke, R. J. Walters, G. P. Summers, and T. Jordan. Proton nonionizing energy loss (NIEL) for device applications. *IEEE Transactions on Nuclear Science*, 50(6):1924–1928, December 2003.

[40] S. Agostinelli, J. Allison, K. Amako, J. Apostolakis, H. Araujo, P. Arce, M. Asai, D. Axen, S. Banerjee, G. Barrand, F. Behner, L. Bellagamba, J. Boudreau, L. Broglia, A. Brunengo, H. Burkhardt, S. Chauvie, J. Chuma, R. Chytracek, G. Cooperman, G. Cosmo, P. Degtyarenko, A. Dell'Acqua, G. Depaola, D. Dietrich, R. Enami, A. Feliciello, C. Ferguson, H. Fesefeldt, G. Folger, F. Foppiano, A. Forti, S. Garelli, S. Giani, R. Giannitrapani, D. Gibin, J.J. Gómez Cadenas, I. González, G. Gracia Abril, G. Greeniaus, W. Greiner, V. Grichine, A. Grossheim, S. Guatelli, P. Gumplinger, R. Hamatsu, K. Hashimoto, H. Hasui, A. Heikkinen, A. Howard, V. Ivanchenko, A. Johnson, F.W. Jones, J. Kallenbach, N. Kanaya, M. Kawabata, Y. Kawabata, M. Kawaguti, S. Kelner, P. Kent, A. Kimura, T. Kodama, R. Kokoulin, M. Kossov, H. Kurashige, E. Lamanna, T. Lampén, V. Lara, V. Lefebure, F. Lei, M. Liendl, W. Lockman, F. Longo, S. Magni, M. Maire, E. Medernach, K. Minamimoto, P. Mora de Freitas, Y. Morita, K. Murakami, M. Nagamatu, R. Nartallo, P. Nieminen, T. Nishimura, K. Ohtsubo, M. Okamura, S. O'Neale, Y. Oohata, K. Paech, J. Perl, A. Pfeiffer, M.G. Pia, F. Ranjard, A. Rybin, S. Sadilov, E. Di Salvo, G. Santin, T. Sasaki, N. Savvas, Y. Sawada, S. Scherer, S. Sei, V. Sirotenko, D. Smith, N. Starkov, H. Stoecker, J. Sulkimo, M. Takahata, S. Tanaka, E. Tcherniaev, E. Safai Tehrani, M. Tropeano, P. Truscott, H. Uno, L. Urban, P. Urban, M. Verderi, A. Walkden, W. Wander, H. Weber, J.P. Wellisch, T. Wenaus, D.C. Williams, D. Wright, T. Yamada, H. Yoshida, and D. Zschiesche. Geant4—a simulation toolkit. *Nuclear Instruments and Methods in Physics Research Section A: Accelerators, Spectrometers, Detectors and Associated Equipment*, 506(3):250 – 303, 2003.

[41] Thomas Vasileiou and Leopold Summerer. A biomimetic approach to shielding from ionizing radiation: The case of melanized fungi. *PLOS ONE*, 15(4):e0229921, 2020.

[42] Natasha Gruginskie, Federica Cappelluti, Gerard J. Bauhuis, Peter Mulder, Erik J. Haverkamp, Elias Vlieg, and John J. Schermer. Electron radiation-induced degradation of GaAs solar cells with different architectures. *Progress in Photovoltaics: Research and Applications*, 28(4):266–278, 2020.

[43] Francesco Biscani and Dario Izzo. A parallel global multiobjective framework for optimization: pagmo. *Journal of Open Source Software*, 5(53):2338, 2020.

[44] S. R. Messenger, E. M. Jackson, J. H. Warner, and R. J. Walters. SCREAM: A new code for solar cell degradation prediction using the displacement damage dose approach. In *2010 35th IEEE Photovoltaic Specialists Conference*, pages 001106–001111. IEEE, 2010.

[45] Scott R. Messenger, Justin Lorentzen, Robert J. Walters, Jeffrey H. Warner, and Geoffrey P. Summers. Electron to proton damage correlation in space solar cells. In *2006 IEEE 4th World Conference on Photovoltaic Energy Conference*, volume 2, pages 1781–1784, May 2006. ISSN: 0160-8371.

[46] Atikur Rahman, Ahsan Ashraf, Huolin Xin, Xiao Tong, Peter Sutter, Matthew D. Eisaman, and Charles T. Black. Sub-50-nm self-assembled nanotextures for enhanced broadband antireflection in silicon solar cells. *Nature Communications*, 6(1), January 2015.

[47] Jung Woo Leem, Jae Su Yu, Dong-Hwan Jun, Jonggon Heo, and Won-Kyu Park. Efficiency improvement of III–V GaAs solar cells using biomimetic TiO2 subwavelength structures with wide-angle and broadband antireflection properties. *Solar Energy Materials and Solar Cells*, 127:43–49, August 2014.

[48] P. Spinelli, B. Macco, M. A. Verschuuren, W. M. M. Kessels, and A. Polman. Al2O3/TiO2 nano-pattern antireflection coating with ultralow surface recombination. *Applied Physics Letters*, 102(23):233902, 2013.

[49] Young Min Song, Yonkil Jeong, Chan Il Yeo, and Yong Tak Lee. Enhanced power generation in concentrated photovoltaics using broadband antireflective coverglasses with moth eye structures. *Optics Express*, 20(106):A916–A923, November 2012.

[50] G. J. Parker, M. D. B. Charlton, M. E. Zoorob, J. J. Baumberg, M. C. Netti, and T. Lee. Highly engineered mesoporous structures for optical processing. *Philosophical Transactions of the Royal Society A: Mathematical, Physical and Engineering Sciences*, 364(1838):189–199, nov 2005.

[51] Sameia Zaman, Sameia Zaman, Mohammad Muntasir Hassan, Mohammad Muntasir Hassan, Mohammad Muntasir Hassan, M. Hasanuzzaman, and Md Zunaid Baten. Coscinodiscus diatom inspired bi-layered photonic structures with near-perfect absorptance accompanied by tunable absorption characteristics. *Optics Express*, 28(17):25007–25021, 2020.

[52] A. Mellor, N. P. Hylton, S. A. Maier, and N. Ekins-Daukes. Interstitial light-trapping design for multi-junction solar cells. *Solar Energy Materials and Solar Cells*, 159:212–218, 2017.

[53] S. R. Messenger, E. A. Burke, R. J. Walters, J. H. Warner, G. P. Summers, and T. L. Morton. Effect of omnidirectional proton irradiation on shielded solar cells. *IEEE Transactions on Nuclear Science*, 53(6):3771–3778, December 2006.

[54] S. I. Maximenko, M. P. Lumb, J. Moore, L. C. Hirst, M. K. Yakes, and P. P. Jenkins. Thin GaAs solar cells for high irradiation levels. In *46th Photovoltaic Specialists Conference (PVSC)*, pages 2814–2817, June 2019.

[55] Scott R. Messenger, Frankie Wong, Bao Hoang, Cory D. Cress, Robert J. Walters, Craig A. Kluever, and Glenn Jones. Low-thrust geostationary transfer orbit (LT2GEO) radiation environment and associated solar array degradation modeling and ground testing. *IEEE Transactions on Nuclear Science*, 61(6):3348–3355, 2014.

[56] Mher Ghulinyan. One-dimensional photonic quasicrystals. In Lorenzo Pavesi and Mher Ghulinyan, editors, *Light Localisation and Lasing: Random and Quasi-random Photonic Structures*, pages 99–129. Cambridge University Press, Cambridge, 2014.

[57] V. A. Tolmachev, T. S. Perova, and R. A. Moore. Method of construction of composite one-dimensional photonic crystal with extended photonic band gaps. *Optics Express*, 13(21):8433–8441, October 2005. Publisher: Optical Society of America.

[58] Hongqiang Li, Hong Chen, and Xinjie Qiu. Band-gap extension of disordered 1D binary photonic crystals. *Physica B: Condensed Matter*, 279(1):164–167, 2000.

[59] S. G. Tikhodeev, A. L. Yablonskii, E. A. Muljarov, N. A. Gippius, and Teruya Ishihara. Quasiguided modes and optical properties of photonic crystal slabs. *Physical Review B*, 66(4):045102, 2002.

[60] Stephen J. Fonash. *Solar cell device physics*. Elsevier, second edition, 2010.

[61] M. Sotoodeh, A. H. Khalid, and A. A. Rezazadeh. Empirical low-field mobility model for III-V compounds applicable in device simulation codes. *Journal of Applied Physics*, 87(6):2890–2900, February 2000.

[62] Anton V. Ivantchenko, Vladimir N. Ivanchenko, Jose-Manuel Quesada Molina, and Sebastien L. Incerti. Geant4 hadronic physics for space radiation environment. *International Journal of Radiation Biology*, 88(1-2):171–175, January 2012.

[63] M. J. Boschini, C. Consolandi, M. Gervasi, S. Giani, D. Grandi, V. Ivanchenko, P. Nieminem, S. Pensotti, P. G. Rancoita, and M. Tacconi. Nuclear and non-ionizing energy-loss of electrons with low and relativistic energies in materials and space enviroment. In *Astroparticle, Particle, Space Physics and Detectors for Physics Applications*, pages 961–982. World Scientific, 2012.

[64] V. N. Ivanchenko, O. Kadri, M. Maire, and L. Urban. Geant4 models for simulation of multiple scattering. *Journal of Physics: Conference Series*, 219(3):032045, April 2010.

[65] D. Heynderickx, B. Quaghebeur, J. Wera, E. J. Daly, and H. D. R. Evans. New radiation environment and effects models in the European Space Agency's Space Environment Information System (SPENVIS). *Space Weather*, 2(10), 2004.